Fatigue behavior and tribological properties of laser additive manufactured aluminum alloy/boron nitride nanosheet nanocomposites

Chen, C., Araby, S., Demiral, M., Cai, R., Yang, X., Wang, W. & Meng, Q.

DOI 10.1016/j.jmrt.2022.08.124
ISSN 2238-7854

Publisher: Elsevier

Available online at www.sciencedirect.com

jmr&t Journal of Materials Research and Technology

journal homepage: www.elsevier.com/locate/jmrt

Original Article

Fatigue behavior and tribological properties of laser additive manufactured aluminum alloy/boron nitride nanosheet nanocomposites

Caiying Chen [a,d], *Sherif Araby* [b,*], *Murat Demiral* [c], *Rui Cai* [d], *Xuanyi Yang* [e], *Wei Wang* [e], *Qingshi Meng* [a,**]

[a] College of Aerospace Engineering, Shenyang Aerospace University, Shenyang 110136, China
[b] School of Engineering and Digital Sciences, Nazarbayev University, Nur-Sultan 010000, Kazakhstan
[c] College of Engineering and Technology, American University of the Middle East, Kuwait
[d] School of Mechanical, Aerospace and Automotive Engineering, Coventry University, Coventry, United Kingdom
[e] Key Laboratory of Fundamental Science for National of Aeronautical Digital Manufacturing Process, Shenyang 110136, China

ARTICLE INFO

Article history:
Received 3 May 2022
Accepted 25 August 2022
Available online 31 August 2022

Keywords:
Aluminum matrix composites
Laser metal deposition
Ball milling
Wear resistance
Fatigue performance
XFEM

ABSTRACT

Laser additive manufacturing is a promising approach to prepare near-neat shape parts from Al nanocomposites with high mechanical and tribological properties. Owing to its lubricious nature, boron nitride nanosheets (BNNSs) were added into AlSi10Mg alloy *via* high-speed ball milling and laser metal deposition (LMD) to manufacture self-lubricating Al alloy nanocomposites with outstanding wear resistance and fatigue performance. The study shows that number of cycles-to-failure due to tensile fatigue increased from 10^3 for pure AlSi10Mg to 10^6 upon adding only 0.1 wt% of BNNSs. At 0.2 wt% BNNSs, the friction coefficient and wear-out volume of AlSi10Mg alloy decrease by 58% and 57%, respectively. Scanning electron microscopy micrographs show that pure AlSi10Mg has a worn surface of grooves, wide ridges, debris and large protrusions of worn material along the groove edges. The wear mechanism is mainly plastic deformation, delamination and adhesion in pure AlSi10Mg. On the other hand, the LMD-built AlSi10Mg/BNNS composites exhibit less rough surface with clear wear trails due to the thin lubricant layer formed from the extruded BNNSs during the test. An extended finite element model for the crack propagation during fatigue testing is developed, where the obtained results are in accord with the experimental measurements. The present study shows that additive manufacturing technology is capable to fabricate Al matrix composites with tailored properties for various design applications.

* Corresponding author. School of Engineering and Digital Sciences, Nazarbayev University, Nur-Sultan 010000, Kazakhstan
** Corresponding author. College of Aerospace Engineering, Shenyang Aerospace University, Shenyang 110136, China
E-mail addresses: Sherif.gouda@nu.edu.kz (S. Araby), mengqingshi@hotmail.com (Q. Meng).

https://doi.org/10.1016/j.jmrt.2022.08.124

1. Introduction

The demand for high-performance alloys in aerospace, military and automotive industries has been significantly increased in the last decade [1]. Metal matrix composites combine excellent properties of metal and reinforcing fillers, demonstrating distinctive properties including high strength, high ductility and outstanding fatigue performance [2]. Among the numerous reported metal-based composites, Al matrix composites (AMCs) are brought to the forefront due to their high mechanical performance, low density, high stiffness and specific strength. AMCs are widely used in drone shell, car body, aerospace engine and spacecraft's body [3] where lightweight and ductility along with high strength are needed. Ceramic fillers were extensively used in reinforcing AMCs such as TiC [4], TiB_2 [4,5] and TiN [6]. Investigating tribological properties and fatigue performance of AMCs are crucial for applications where dynamic load and friction between moving parts are the nature of service such as aerospace and automotive industry.

It is known that processing methods and filler types determine the level of reinforcement in AMCs for both tribological properties and fatigue performance. Sujith et al. [7] used stir casting to prepare Al-7079/TiC composites and studied their wear resistance, at 9 wt% TiC particles, the friction coefficient and wear weight loss reduced by 18% and 40%, respectively compared to pure Al alloy. Al 2024 alloy/TiB_2 nanocomposites were prepared *via* mixed salt reaction method [8], at 4.17 vol% of TiB_2, the fatigue limit of the composite was 24.13% higher than base matrix when the stress ratio was 0.1. Although conventional methods are well-established in metallic composites, they face challenges in developing high strength and yet ductile metal nanocomposites. For example, stir casting process faces a challenge in achieving uniform nanofiller dispersion in the matrix due to poor wettability and high viscosity. Long stirring time is essential to obtain uniform dispersion which exposes the matrix for the risk of oxidation, in particular for metals such as Al-based alloys. Moreover, flexibility in customizing products is limited *via* conventional methods. Additive manufacturing presents a promising approach to fabricate a near-net shape and customized products from metal nanocomposites with complex and high mechanical properties [9]. Laser metal deposition (LMD) is one of the powder-based additive manufacturing processes that uses focused thermal energy provided by a laser beam in fusing and bonding metal particles to create neat-net shape components [10]. LMD leads to a product with fine grains and dense structures at rapid melting and solidification rates. This improves the mechanical performance of final product. In terms of economic benefits, complex-shaped components can be formed as a whole by LMD without production or assembly molds. Consequently, the savings from LMD are numerous including (i) the production of different profiles and dimensions with minimum set-up time (ii) less labor force and workload involved in the assembly process and (iii) less post processes after production. Therefore, although LMD is not suitable for large-scale production, it possesses an economical value in comparison with traditional methods in producing customized parts at small-scale production.

Plethora studies reported additive manufacturing to prepare metal matrix nanocomposites [4,5,11–13]. Wang et al. [11] developed strong and ductile Al alloy nanocomposites reinforced by graphene platelets *via* LMD. Their nanocomposite possessed increments of 23% in Young's modulus, 60.7% in ultimate tensile strength and 194% in ductility. In another work [13], LMD was used to synthesis AlSi7Mg/graphene oxide. These composites showed improvements in all properties including hardness, tensile strength, ductility, modulus of elasticity and yield strength upon adding low content of graphene oxide. Selective laser melting (SLM) process was employed to fabricate AlSi10Mg/TiN nanocomposites [6], adding 4 wt% of TiN endowed AlSi10Mg matrix maximum tensile strength (492 ± 5.5 MPa), ductility (7.5% ± 0.29) and microhardness (157 ± 4.9 HV). In another study [4], AMCs reinforced by TiB_2 and TiC *via* SLM. When both fillers were added together (TiB_2+TiC) into AlSi10Mg alloy, the nanocomposite showed increments of 40.3% in ultimate tensile strength and 166.7% in ductility in comparison with pure AlSi10Mg. Li et al. [5] studied the mechanical properties of nano-TiB_2 decorated AlSi10Mg composite manufactured by SLM, the nanocomposites showed high ultimate tensile strength of ~530 MPa, excellent ductility of ~15.5% and high microhardness of 191 $HV_{0.2}$. Coefficient of thermal expansion (CTE) and thermal conductivity of 3D-printed AlSi10Mg composites were changed upon adding graphene. CTE was reduced by 10%, thermal conductivity slightly increased of AlSi10MG after adding 0.1 wt% of graphene [14]. Though there are some reports on fatigue strength and its associated fracture behavior of 3D-printed Al alloys [15,16], there are rare studies on fatigue performance and tribological properties of Al- alloys nanocomposites prepared by LMD. In fact, to the best of our knowledge, there is no study on fatigue performance or wear properties of 3D-printed Al alloy reinforced by boron nitride nanosheets (BNNSs). Since LMD succeeded in developing Al alloy/graphene nanocomposites with higher quasi-static mechanical performance in comparison with conventional methods, our hypothesis is that LMD can be used to prepare Al alloy/BNNS nanocomposites with high fatigue life and enhanced tribological properties, taking the advantage of lubricious nature, high strength and thermal stability of BNNSs [17,18].

In the present work, AlSi10Mg/BNNS nanocomposites were fabricated by LMD process assisted by high-speed wet-ball milling. BNNSs were added into AlSi10Mg alloy within range 0–0.2 wt%. Fatigue life of the properad samples and their corresponding fracture mechanism were investigated. Tribological properties including wear rate and friction coefficient of the prepared Al alloy/BNNS nanocomposites were studied and compared to pure Al alloy. Moreover, we developed a finite element model to simulate the fatigue tensile test of pure AlSi10Mg and a material representing AlSi10Mg/BNNS composite, the model was able to show the effects of BNNSs on the crack propagation rate during fatigue loading.

Table 1 – Nominal chemical composition of AlSi10Mg powder.

Element	Al	Si	Mg	Mn	Fe	Cu	Ni	Zn	Sn	Pb	Ti
Content (wt%)	Bal.	9–10	0.4–0.48	< 0.1	< 0.25	< 0.05	< 0.05	< 0.01	< 0.05	< 0.02	< 0.005

2. Material and experimental details

2.1. Materials

- AlSi10Mg powder (10 wt% Si and 0.4 wt% Mg, 100–150 μm in size, purity >99%) was supplied from *Nantong Heyuan Intelligent Technology Co., LTD*, China. The chemical composition of the AlSi10Mg is listed in Table 1. Fig. 1 shows SEM micrograph of as-received AlSi10Mg powder.
- Hexagonal boron nitride sheets (h-BN) with 30–50 nm in thickness and purity >99.9% was purchased from *Shanghai Chaowei Nanotechnology Co., LTD*, China.

2.2. AlSi10Mg/BNNS nanocomposite preparation

The fabrication process of the AlSi10Mg/BNNS nanocomposite includes the following steps. A predetermined h-BN was ultrasonicated in 60 ml ethanol for 2 h. After sonication, h-BN is delaminated into few-layer boron nitride nanosheets (BNNSs). BNNSs are blended with AlSi10Mg powder using a planetary wet-ball mill (*Hunan Focucy Technology Co., LTD*, China) in the presence of 60 ml of alcohol. The operation parameters of wet-ball mill process are presented in Table 2. After ball milling, the remnants on the balls' surface and container's wall were carefully collected *via* alcohol washing and added to the saved composite powder. This ensures the mass fraction of BNNSs before and after ball milling are the same. The blended powder was dried in an oven overnight at 80 °C to remove any traces of alcohol. Subsequently, the AlSi10Mg/BNNS powder is ready for laser metal deposition (LMD) process. ZL104 aluminum alloy was used as the substrate for LMD process. The substrate was ground and cleaned with ethanol before the LMD process.

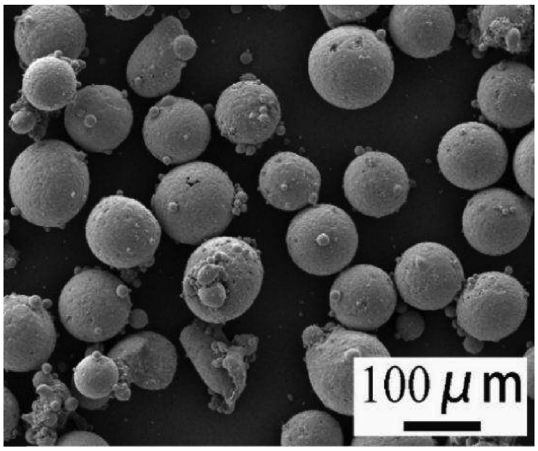

Fig. 1 – SEM image of AlSi10Mg powder.

The LMD machine used in this study belongs to the *National defense key discipline laboratory*, Shenyang Aerospace University, China. It consists of coaxial powder feeding and interrepublic group (IPG) fiber laser systems with maximum power output of 6 kW. A schematic diagram of LMD process in preparing AlSi10Mg/BNNS nanocomposite is presented in Fig. 2. The LMD process was carried out under the protection of argon gas, the oxygen concentration was maintained at < 50 ppm and the operation parameters are summarized in Table 3. As per definition, laser energy density is the energy input by laser to a unit volume within the LMD process, it can be calculated using [19]:

$$\psi = \frac{P}{u \times h \times d} \quad (1)$$

where ψ is density of laser energy (J/mm^3), P is the power (W), u is the scanning speed (mm/s), h and d are the hatch space (mm) and height of each deposition (mm), respectively. Using the process parameters provided in Table 3, accordingly, the energy density is calculated as 285 J/mm^3. It is noteworthy to mention that the layer thickness is not a direct controllable parameter in LMD process. It depends on the scanning speed, feed rate of powder quantity and the absorption rate. The latter is a material property. During LMD process, the scanning speed and powder feed rate were set at 5 mm/s and 2 g/s, respectively. The control panel of LMD machine accordingly records the thickness of already-printed layer at ~0.7 mm.

LMD parts are prepared layer by layer, consequently, the heat of the previously formed layer gradually accumulates in the alloy during the deposition process. Therefore, a reciprocating scanning method was used to help in heat dissipation from the alloy and prevent thermal buckling deformation in the LMD-prepared parts. The path of 3D printing *via* LMD is shown in Fig. 3a. AlSi10Mg nanocomposites were LMD-printed at 0, 0.05, 0.1 and 0.2 wt% BNNSs and they were named AlSi10Mg, 0.05AlSi10Mg/BNNS, 0.1AlSi10Mg/BNNS and 0.2 AlSi10Mg/BNNS, respectively.

2.3. Fatigue test

The specimens of LMD-printed AlSi10Mg/BNNS nanocomposite for fatigue test were sized in accordance to international standard of ASTM E466-2015 [20]–Fig. 3b. Prior to the fatigue test, all samples were mechanically polished with sandpapers along the longitudinal to smooth the surface and profusely washed with distilled water afterwards. This would prevent premature crack propagation from large apparent scratches [21]. Fatigue test was carried out by Instron 50 kN servo-hydraulic fatigue testing system. The fatigue test was performed at room temperature (RT). The stress ratio was set at $R = 0.06$ and frequency of 15 Hz, the type of cyclic stress was pulse type under tensile–tensile loading mode. Four samples at each BNNSs fraction were tested to calculate the average of

Table 2 – Parameters of ball milling Al alloy powder with BNNSs.

Ball milling parameters	Value
Ball size (mm)	5
Milling solvent	Anhydrous ethanol
Rotation speed of main disk (rpm)	320
Milling time (hr)	16
Ball-to-powder weight ratio	5:1
Milling mode	30 min ball milling followed by 8 min interval time

fatigue life. Fractographic analyses were performed using the scanning electron microscope (SEM) *Quanta* 2580 FEG.

2.4. *Wear test*

Wear test was conducted according to the standard of GB/T 12444-2006 [22] using a reciprocating friction wear testing machine (*Lanzhou Zhongke Kaihua Technology Development Co., LTD*, China) at RT. Specimens for wear test were prepared from LMD-3D printed AlSi10Mg/BNNS nanocomposites by wire electro-discharge machining, the samples were cut to a square cross-section of 10 × 10 mm and thickness of 4 mm. The samples were embedded in metallographic inlaid powder and prepared using a metallographic specimen inlaying mechanism (*Shanghai Yanrun Optical Machine Technology Co., LTD*. China) in the form of Φ 30 × 10 mm blocks. A spherical zirconium oxide indenter with hardness >90 HRA was used as sliding friction substrate. The wear test was set at condition of 5 N for the load, 200 rpm for the sliding speed and 5 mm for the sliding distance. The speed and load were further increased to 500 rpm and 20 N on a group of 0.2AlSi10Mg/BNNS nanocomposites in comparison with AlSi10Mg. No lubricant was used during the wear test. Prior to the wear test, all the contact surfaces were ground and mechanically polished following standard procedures (600, 800 and 1000 grit emery papers) to eliminate any scratch or dirt. Each friction pair was cleaned in acetone before and after the wear test. Parameters including friction coefficient, wear volume loss, wear rate and wear depth were measured. The wear rate (w) of the composite was calculated by the formula $w = V/PL$, where V, P and L represent the wear volume (mm^3), applied load (N) and total sliding distance (m), respectively. The friction coefficient and wear rates were the average values of four replicates.

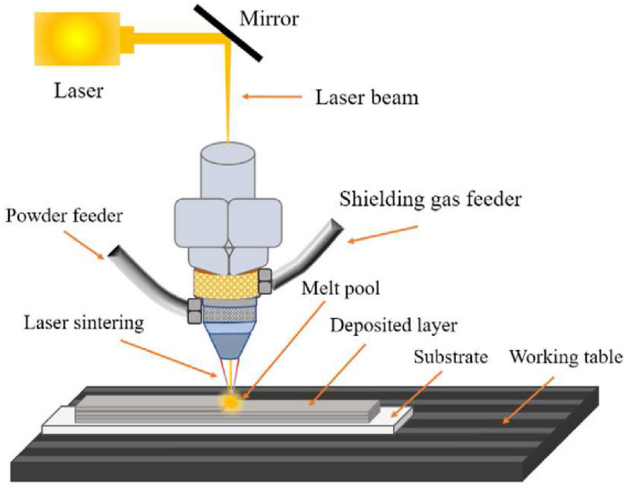

Fig. 2 – Schematic diagram of laser metal deposition process.

2.5. *Morphology characterization*

High resolution transmission electron microscope (HRTEM, *FEI Talos, America*) was used to observe the morphology of h-BN nanosheets (BNNSs) and atomic force microscope (AFM, *Dimension Icon, Germany*) to measure their thickness. For both observations, the sample was prepared by sonication and sequential dilution till 0.0004% of BNNSs in acetone. Few droplets of BNNSs suspension were placed on a 200-mesh copper grid and dried for TEM imaging. Other droplets were on a silicon wafer for AFM measurements. The morphology of AlSi10Mg/BNNS mixed powder and microstructure of the AlSi10Mg/BNNS composites were observed by scanning electron microscope (SEM, *su8010, Hitachi, Japan*), as well as the fatigue fracture surfaces.

3-dimensional (3D) morphology of the wear track was observed by a 3D surface profilometer using an optical surface measurement system (*Leica DCM8, Germany*). In addition, SEM was used to study the microstructures of the LMD-manufactured samples and to analyze the morphologies of the wear surfaces after sliding tests.

3. Results and discussion

3.1. *Morphology of h-BN nanosheets*

HRTEM micrographs in Fig. 4(a–b) show that BNNSs have a typical plate-like structure of layers stacked together rather than monolayers. An interplanar spacing of 0.33 nm is associated with diamond hexagonal BN on (003) plane corresponding to PDF card (ICDD Card No. 45-1171) [23]. AFM was employed to directly measure the thickness of BNNSs, twenty randomly selected nanosheets were measured. Representative 3D and 2D morphologies of six measurements are shown in Fig. 4(c–d). The average thickness of BNNSs is recorded at 4.31 ± 0.21 nm. Since single layer of hexagonal boron nitride is approximately 0.4–0.5 nm [24,25], the average number of layers in BNNSs is 8–10 layers. It is noteworthy that the thickness range of the as-received h-BN was 30–50 nm, it was measured and reported in previous works [26]. Upon sonication, the stacked sheets are able to exfoliate and delaminate into thinner sheets as evident by TEM and AFM measurements.

Table 3 – LMD processing parameters of AlSi10Mg/BNNS composites.

LMD processing parameters	Value
Laser power (W).	2000
Laser spot diameter (mm)	4
Hatch space (mm)	2
Scanning speed (mm/s)	5
Powder-feeding speed (g/min)	2
Height of each layer (mm)	0.7
Printing direction	z-axis

3.2. *Phase compositions and microstructure of the AlSi10Mg/BNNS composites*

Fig. 5(a–f) presents SEM micrographs of AlSi10Mg powder with 0.05–0.2 wt% BNNSs after wet-ball milling at two magnifications. The SEM images show that all the composite powders preserved their sphericity after ball milling. BNNSs are uniformly dispersed and attached onto the AlSi10Mg powder after 16 h of high-energy ball milling. Spherical or nearly spherical mixed powder is conducive to printing high-density metal matrix composites by LMD process [27]. With the increase of BNNS content, more BNNSs are attached onto AlSi10Mg powder and hence a few sheets begin to agglomerate as shown in Fig. 5f for 0.2 wt% BNNSs. In wet high-energy ball milling, the existence of alcohol effectively reduced the high temperature generated during the milling process and helped to have a cold bonding interface between BNNSs and AlSi10Mg powder. Random and uniform dispersion of BNNSs with good bonding into the matrix support maintaining uniform properties as well as high functional properties of the composites.

Fig. 6 displays the microstructural images and energy dispersive X-ray spectroscopy (EDS) analysis of pure LMD-built AlSi10Mg. In Fig. 6a, the microstructure of pure AlSi10Mg (0 wt%) contains two phases: (i) Al–Si eutectic as bright white particles and (ii) α-Al dendrite in grey [10]. Al–Si eutectic particles undergo spheroidizing, thereby the mechanical properties of the material are improved. This is consistent with the microstructure of AlSi10Mg alloy prepared by Fei et al. [28] using LMD. EDS elemental analysis in Fig. 6(b–d) shows that Al, Si and Mg elements evenly exist in the alloy. Also, crude columnar dendritic structure is evident from the EDS image in Fig. 6c.

Fig. 7 shows the microstructure of LMD-built 0.1AlSi10Mg/BNNS composite that comprises of Al–Si eutectic and α-Al dendrite. Compared to pure AlSi10Mg (Fig. 6), adding BNNSs improved the microstructure of composites. The Al–Si eutectic and α-Al dendrite structures of the composites became smaller and dense as presented in Fig. 7a, this is in favour to reinforcing the matrix. EDS elemental analysis in Fig. 7(b–e) show that BNNSs are uniformly dispersed within the Al alloy matrix predicting a high mechanical performance of composites. Furthermore, the EDS mapping in Fig. 7(b–c) shows that Al–Si eutectic in 0.1AlSi10Mg/BNNS composite is interconnected network-structure with fine columnar dendritic structure in regular and dense manner. In addition, BNNSs are dispersed homogeneously and densely over the surface of aluminium matrix, as shown in Fig. 7(d–e).

The microstructure of LMD-built surface structure is further observed by magnifying region A in Fig. 7a as shown in Fig. 7(f–h). Eutectic precipitation (Al–Si eutectic, the red arrow) is sharply defined, forming a strong network structure of columnar dendrites. The boundary is decorated with fibrous silicon particles (rectangle with red dotted line). This structure is mainly due to two reasons: (i) since the melting point of the aluminium alloy (837 K) is low, the Al alloy was rapidly melted under the focused and high energy laser beam at temperature of 2700 K; and (ii) the speed of solidifying and cooling is very fast during this process because of the localised melting pool. In the solidification process of AlSi10Mg, the Si phase first solidified into a solid phase at the front of the solid/liquid interface, then it was expelled from the liquid phase. The solubility of Si in liquid increased due to the fast-cooling rate. After Si reached supersaturation in Al matrix, it precipitated and nucleated at the cell boundary [29,30]. Consequently, the Si particles precipitated in Al dendrites and formed Al–Si eutectic (some reports named Si-rich particles [31]).

3.3. *Fatigue strength*

Four groups (four samples in each group) of AlSi10Mg specimens with 0–0.2 wt% BNNSs were prepared and tested to measure fatigue strength. The cross-sectional area, stress amplitude (σ_a), mean stress (σ_m) and the number of cycles of the tested samples are recorded in Table 4. The stress amplitude and mean stress were selected based on the tensile test results of LMD-built AlSi10Mg, 0.05 AlSi10Mg/BNNS, 0.1

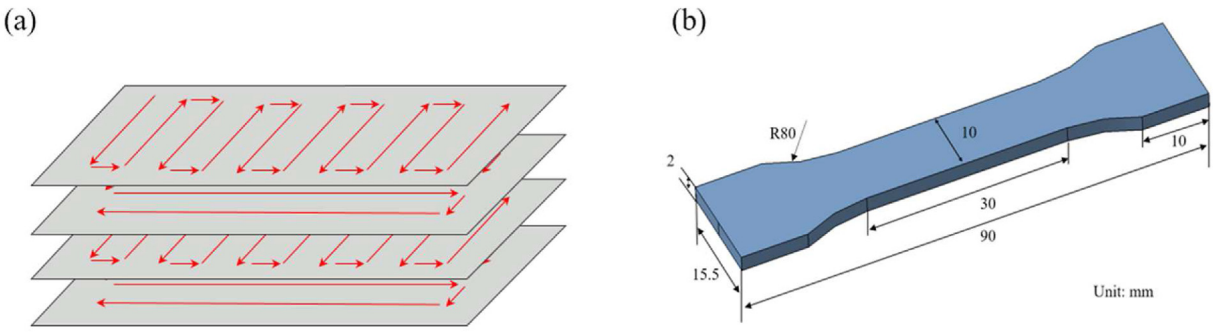

Fig. 3 – (a) 3D printing path *via* LMD and (b) flat dumbbell sample cut by wire electro-discharge machine.

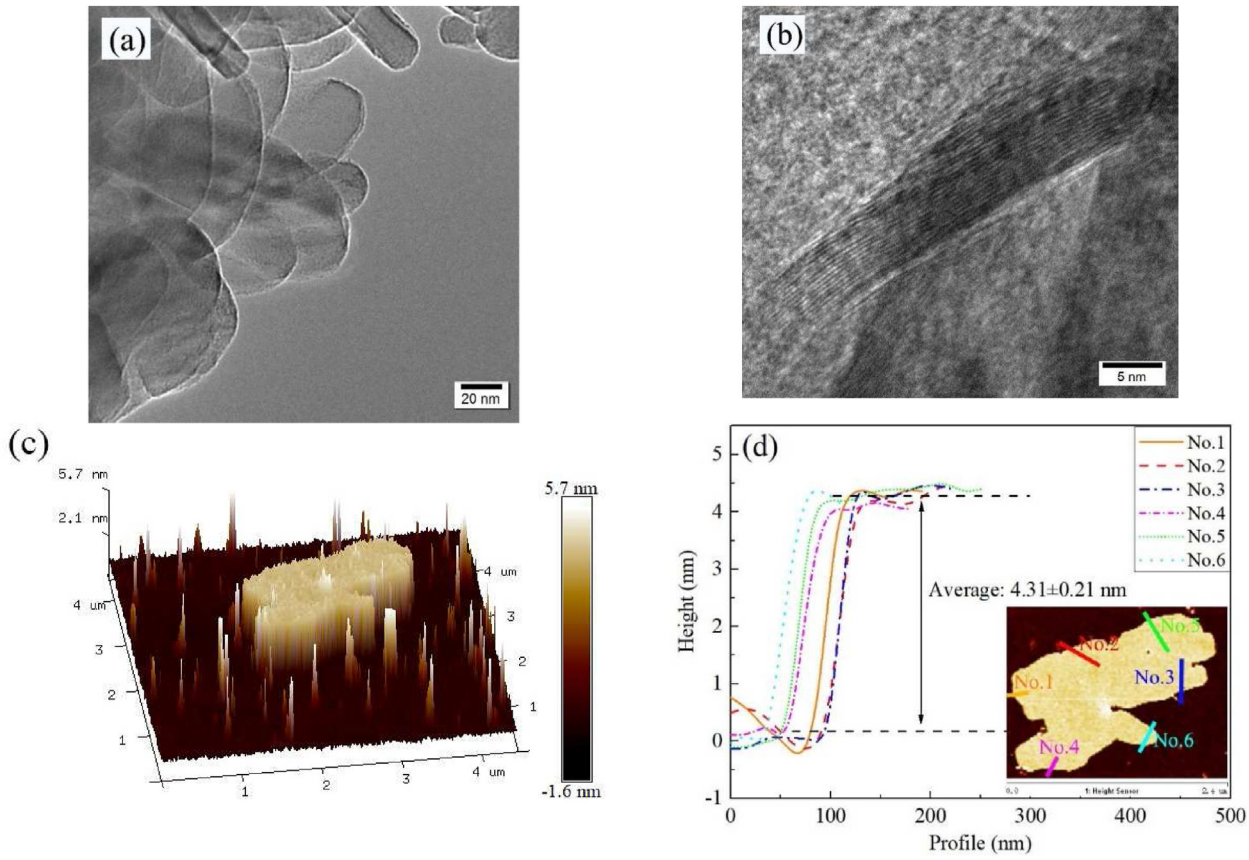

Fig. 4 – Morphology of BNNSs: (a) TEM micrograph, (b) HRTEM micrograph and (c, d) 3D and 2D atomic force microscopic images.

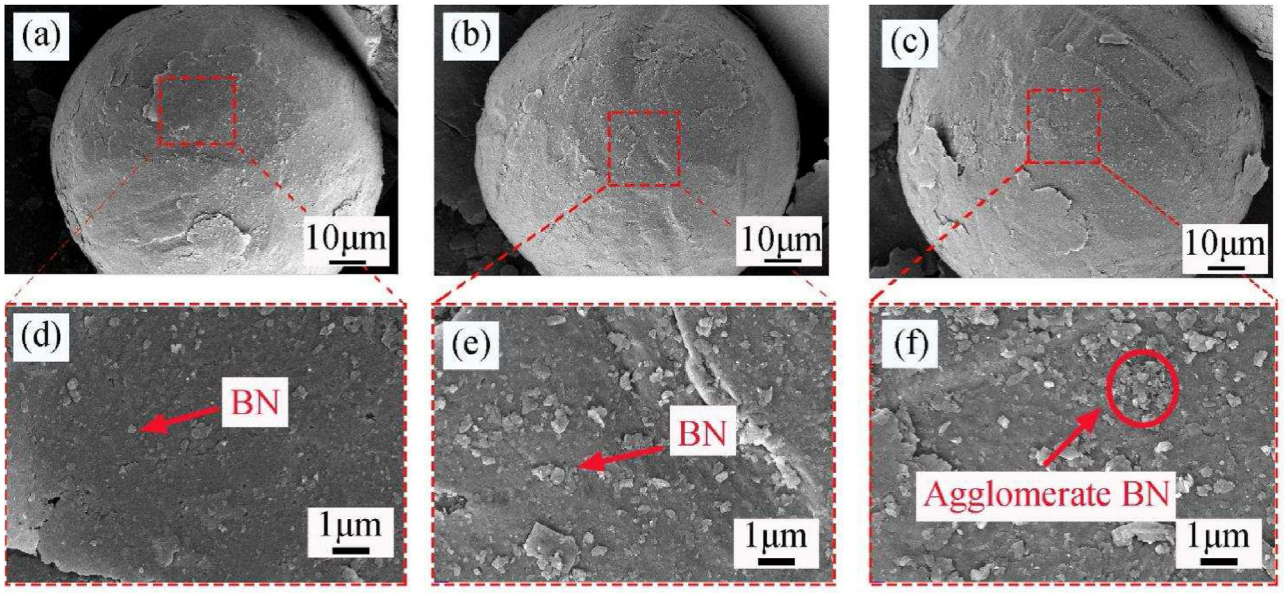

Fig. 5 – SEM micrographs of AlSi10Mg/BNNS powder after ball milling: (a) and (d) for 0.05AlSi10Mg/BNNS mixed powder; (b) and (e) for 0.1 AlSi10Mg/BNNS mixed powder; and (c) and (f) for 0.2 AlSi10Mg/BNNS mixed powder.

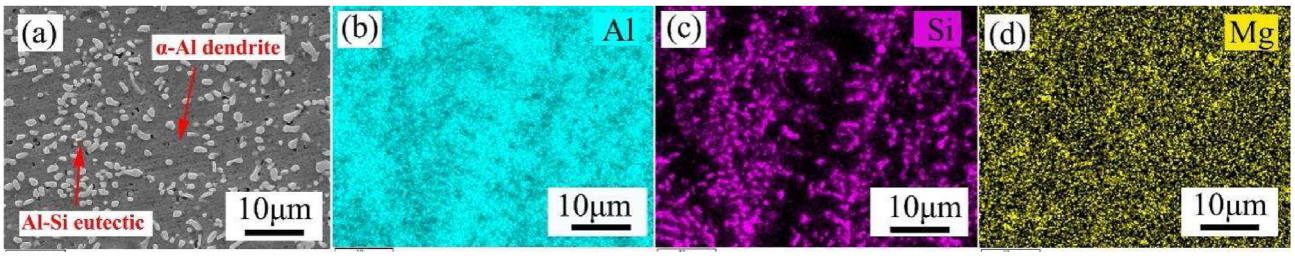

Fig. 6 – (a) SEM image of LMD-built AlSi10Mg material and (b–d) EDS elemental analysis of the corresponding material.

AlSi10Mg/BNNS and 0.2 AlSi10Mg/BNNS specimens as shown in Fig. 8. The relationship between stress amplitude (σ_a) and mean stress (σ_m) is given as follow:

$$\sigma_m = \frac{\sigma_{max} + \sigma_{min}}{2} \quad (2)$$

$$\sigma_a = \frac{\sigma_{max} - \sigma_{min}}{2} \quad (3)$$

where σ_{min} and σ_{max} are the minimum and maximum applied stress, respectively.

The S–N curve of maximum stress and number of cycles-to-failure at various BNNS contents shown in Fig. 9. The number of cycles-to-failure is significantly increased upon adding BNNSs yet at very low content ≤0.2 wt%. For example, LMD-built AlSi10Mg alloy fails after less than 10^4 cycles which belongs to low cycle fatigue. On the other hand, the number of cycles-to-failure of 0.05AlSi10Mg/BNNS and 0.1AlSi10Mg/BNNS specimens reach 10^4 and 10^5, respectively. The maximum stress for both specimens are recorded at 219.31 and 253.56 MPa. When the content of BNNSs increased to 0.2 wt%, the fatigue performance is marginally improved in comparison with 0.1 wt% BNNSs.

The recent works that investigated fatigue performance AMCs prepared by conventional methods are summarized and compared with our current work in Table 5. Hochreiter et al. [32] used hot extrusion to prepare AMCs reinforced by SiC and Al_2O_3 microparticle. The fatigue limit improved by 35.71% compared to the base Al alloy and the fatigue lifetime increased from 10^3 to 10^7 cycle. SiC and Al_2O_3 nanoparticles were used as reinforcing phase in AA7075 alloy *via* stir casting [33]. The fatigue limit increased by 12.13% compared to matrix and the fatigue lifetime increased from 10^5 to 10^7 cycle. In another study, the fatigue limit increased only 8.3% upon adding SiO_2 nanoparticles in Al alloy using stir casting. In comparison to the current work, adding only 0.1 wt% BNNSs to AlSi10Mg alloy increased the fatigue limit by 47% and its lifetime increased from 10^3 to 10^6 cycle which give advantages to both BNNSs as reinforcing filler as well as LMD process over the conventional methods.

Further investigation was conducted *via* numerical analysis to assess the fatigue life of LMD-built Al alloy/BNNS composites. A low cycle fatigue analysis using direct cyclic approach was performed using Abaqus/Standard. The extended finite element method (XFEM) based on linear elastic fracture mechanics was used for the analysis of crack propagation. The initiation and growth of the crack was characterized by using Paris Law linking the fracture energy release rate to crack growth. The Paris regime is confined by (i) the upper limit energy release rate (G_{pl}) above which the fatigue crack propagates at a higher rate, and (ii) the lower limit (G_{thresh}) below which the fatigue crack is unlikely to happen or expand. The values of G_{pl} and G_{thresh} are related to the critical

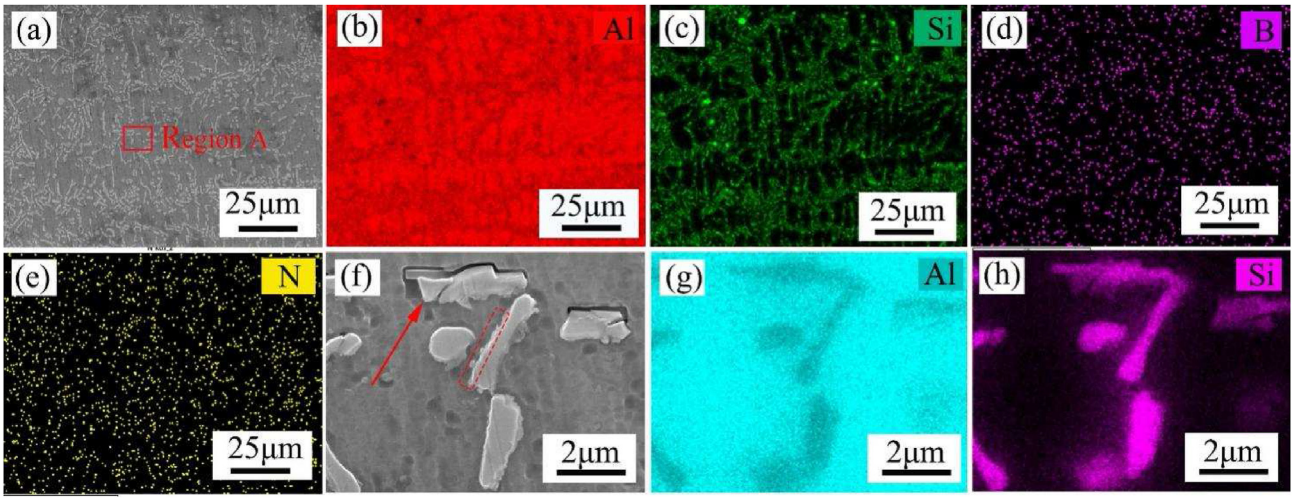

Fig. 7 – (a) SEM image of LMD-built 0.1AlSi10Mg/BNNS composite; (b–e) EDS elemental analysis of the corresponding composite; and (f–h) local enlarged view of region A in Image (a).

Table 4 – Parameters and results of fatigue test on AlSi10Mg alloy and its BNNS composites.

BNNSs (wt%)	Specimen #	Specimen size (cross-section area, mm^2)	σ_a (MPa)	σ_m (MPa)	Number of cycles-to-failure
0	1	20.06	40.60	45.76	5.00×10^3
	2	19.98			1.51×10^3
	3	20.09			5.08×10^3
	4	19.82			3.97×10^3
0.05	5	19.09	51.54	58.12	1.10×10^4
	6	20.11			2.20×10^4
	7	19.89			1.80×10^4
	8	20.07			3.55×10^4
0.1	9	20.09	59.59	67.19	1.00×10^6
	10	19.96			1.67×10^5
	11	20.10			9.98×10^5
	12	20.05			3.00×10^5
0.2	13	20.01	57.516	64.859	1.54×10^5
	14	19.94			1.99×10^5
	15	20.22			7.59×10^5
	16	20.12			3.52×10^5

equivalent strain energy release rate. $G_{eq,c}$ was calculated based on the mode-mix criterion. In the present study, the following linear power law model was used [37]:

$$\frac{G_{eq}}{G_{eq,\,c}} = \left(\frac{G_1}{G_{1c}}\right)^{\alpha_1} + \left(\frac{G_2}{G_{2c}}\right)^{\alpha_2} + \left(\frac{G_3}{G_{1c}}\right)^{\alpha_3} \quad (4)$$

where, G_{1c}, G_{2c} and G_{3c} are the critical energy release rates in Mode I, Mode II, and Mode III. α_1, α_2 and α_3 are taken 1.0. It was assumed that $G_{pl} = 0.85\ G_{eq,\,c}$ and $G_{thresh} = 0.01\ G_{eq,\,c}$ [38].

In the low-cycle fatigue analysis, the onset of the fatigue crack growth is characterized by ΔG as the difference of energy release rates when the structure is loaded with maximum and minimum loading in a cycle. The criterion is defined as $N \geq c_1 \Delta G^{c_2}$, where c_1 and c_2 are material constants and N is the cycle number. Once the onset of crack propagation was fulfilled, its growth rate per cycle was ruled by the Paris Law using relation $da/dN = c_3 \Delta G^{c_4}$, where *a* is the crack length, c_3 and c_4 are material constants [38]. Since, in Abaqus computations, da/dN was characterized in terms of energy release rate instead of stress intensity factor, the definitions of c_3 and c_4 were slightly different than the constants *C* and *m* in the fundamental Paris Law ($da/dN = C\ \Delta K^m$). The constants are related to each other as follows: $c_4 = m/2$ and $c_3 = C\ E^{c_4}$ [39]. It is important to mention that the cyclic energy release rate at maximum loading, G_{max}, should satisfy $G_{max} > G_{thresh}$ and $G_{pl} > G_{max} > G_{thresh}$ in the regions corresponding to the onset and growth of crack, respectively. Once the crack was nucleated, the computations were done as follows: (i) at cycle N, the crack length is recognized as (a_N); and (ii) after incremental number of cycles (ΔN), the crack length is increased by $a_{\Delta N}$, thus the total crack length becomes $a_{N+\Delta N}$ by freeing minimum one element at the interface. The node spacing at the interface elements at the crack tips is defined as $\Delta a_{Nj} = a_{N+\Delta N} - a_N$. Depending on material constants c_3 & c_4 and

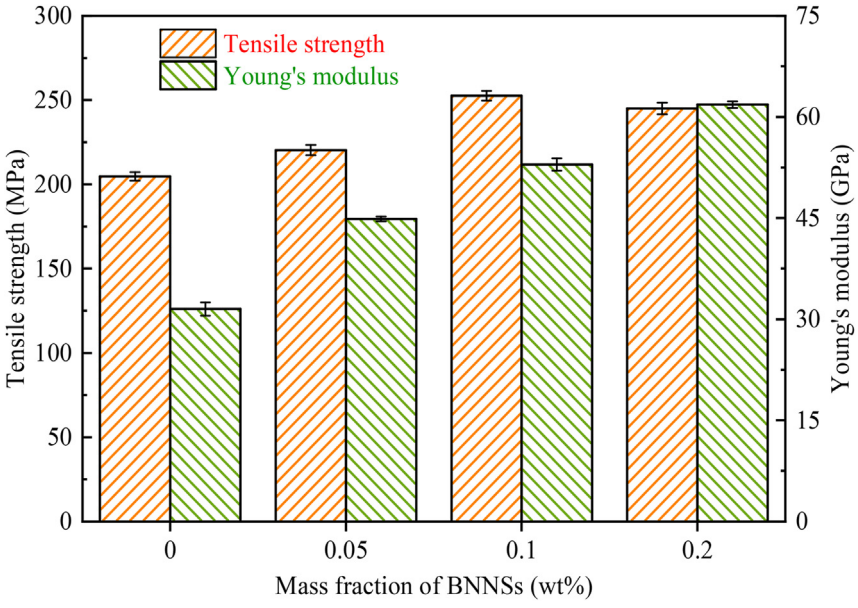

Fig. 8 – Quasi-static tensile properties of AlSi10Mg/BNNS composites.

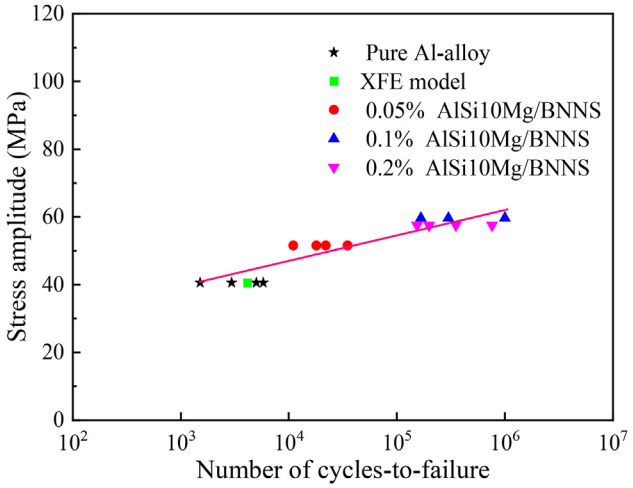

Fig. 9 – Stress amplitude and number of cycles-to-failure of LMD-built Al alloy/BNNS composites.

node spacing at the interface elements at the crack tips, the number of cycles necessary to fail each interface element at the crack tip was calculated as ΔN_j, where j represents the node having the crack tip. The numerical analysis was progressed by freeing at least one interface element after each stabilized loading cycle. Thereby, the number of elements that requires minimum number of cycles is defined and hence released. Herewith, the objective function is defined as $\Delta N_{min} = min\ (\Delta N_j)$ *i.e.* this occurs when number of cycles to propagate the crack to reach an element length of $\Delta a_{Nmin} = \min\ (\Delta a_{Nj})$. Consequently, the most critical element was fully freed with a zero stiffness and a zero constraint at the end of the stabilized cycle. With the release of an interface element, the load was redistributed and a new relative fracture energy release rate was computed for the interface elements at the crack tips for the consecutive cycle [40].

Fig. 10 shows the developed 2D XFEM model of the fatigue tensile test. Its dimensions are identical to those of the experimentally tested samples. While it was fixed from one end, it was stressed from the other end with σ_{max} and σ_{min} at values 86.33 and 5.18 MPa, respectively, corresponding to R = 0.06. The step time for each cycle was 0.066 equivalent to the frequency of 15 Hz. 25 Fourier terms and a time increment of 0.00066 were used for the direct cyclic analysis. Prior to the test, a static step was defined, where σ_{max} was applied to the specimen to introduce a crack at the site of stress concentration. Four-noded plane stress quadrilateral elements (CPS4R) with an element size of approximately 0.3 mm were used in the mesh discretization. Table 6 summarizes the material constants used in the numerical model.

Fig. 11 demonstrates the nucleation and propagation of the crack with an increase in loading cycles obtained using the XFEM simulations. In the pre-defined static loading, two cracks developed at the two edges of the middle section of the specimen. This complied with the study in [43], where the crack initiation in the fatigue tensile test specimen was observed at the region of minimum cross-section and at the corners of the specimen width [43]. It was observed that the onset of crack spread started at N = 1873. Then it propagated along the width direction, where the final fatigue failure occurred at N = 4723. This is in line with the experimentally obtained damage cycle for neat AlSi10Mg where it was ranging between 1500 and 5000 cycles –Table 4.

The experimental results in the current study demonstrate that the fatigue performance of Al–Alloy improved with the addition of BNNSs. The constants of Paris Law were not available in the literature for AlSi10Mg/BNNS composites. In the current study we tried to mimic other composites from the literature to be able to conduct a representative numerical analysis for AlSi10Mg/BNNS composites. The study in [44] investigated the fatigue crack growth properties of neat epoxy and its nanocomposites. The study reported that addition of various nanoparticles decreased the crack propagation, i.e., increased the fatigue life of epoxy. In that study, c_3, c_4 values were presented for the tested materials, where the former parameter got larger and the latter smaller for modified epoxies with nanoparticles when compared to those of neat epoxy. Considering this reference, a representative material model for AlSi10Mg with BNNSs was developed, where its c_3 value was increased from 7.5×10^{-8} to 30.0×10^{-8} while c_4 decreased from 1.75 to 1.25. All other constants were kept constant except Young's modulus (*E*) and σ_{max}, the averages of the measured values for 0.05 wt%, 0.10 wt% and 0.20 wt% BNNS specimens. Fig. 12 compares the crack growth rate for this symbolic material and the pure AlSi10Mg. It is noted that with an addition of BNNSs, the onset of crack propagation is delayed to around 11,010 cycles and fatigue fracture occurs after 34,000 cycles. Also, the crack spread rate substantially decreases in comparison with this of pure Al alloy. This observation is in accordance with the experimental findings presented in Table 4 where the addition of BNNSs nanoparticles improved the cyclic performance of Al alloy. Overall, the 2D XFEM model captured the main features of the fatigue tensile test successfully. In

Table 5 – Published studies on fatigue properties of AMCs reinforced by various fillers *via* traditional methods.

Preparation method	Matrix material	Filler type	Fatigue limit (increase %)	Fatigue lifetime (cycle)	Ref.
Mould casting	Al–Si cast alloy	SiC microparticle	/	from 10^2 to 10^6	[34]
Melt reaction and hot extrusion	AA6111 Al alloy	ZrB_2 nanoparticles	31.5	from 10^5 to 10^7	[35]
Stir casting	AA7075 Al alloy	SiC and Al_2O_3 nanoparticle	12.13	from 10^5 to 10^7	[33]
Hot extrusion	6061 Al alloy	SiC; Al_2O_3 microparticle	35.71	from 10^3 to 10^7	[32]
Ball-milling and stir-casting	AlSi12Cu3Ni2MgFe alloy	SiO_2 nanoparticle	8.26	from 10^3 to 10^4	[36]
Mixed salt reaction	2024 Al alloy	TiB_2 microparticle	24.34	from 10^4 to 10^7	[8]
Laser metal deposition	AlSi10Mg alloy	Boron nitride nanosheets	46.77	from 10^3 to 10^6	This work

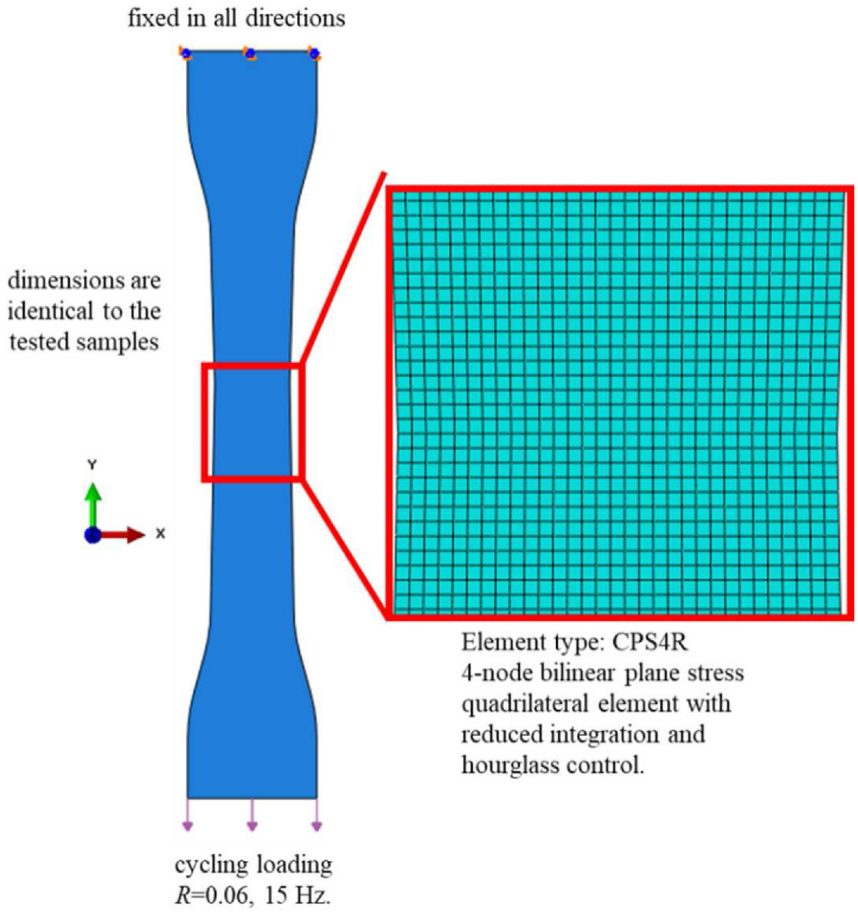

Fig. 10 – XFEM model of tensile test specimen subjected to cyclic loading.

connection with this, the study of Gairola and Jayaganthan [45] demonstrated that the 3D XFEM model of compact tension test of Al 6061 alloy produced similar results when compared to those of 2D XFEM model, while the computation time for the former was approximately 2.5 times of the latter. Similarly, Teimouri et al. [46] simulated the 2D and 3D fatigue delamination in composite laminates under high cycle loading using XFEM. The results were qualitatively similar. Therefore, in the present study, a 2D model was considered to be sufficient to describe the fatigue behavior of the AlSi10Mg/BNNS composite.

Table 6 – Material constants used in the low-cycle XFEM fatigue analysis.

Source	Property	AlSi10Mg	Representative material with BNNSs (mimic AlSi10Mg/BNNS)
This work	E (GPa)	31.5	53.21
[41]	υ	0.3	0.3
This work	σ_{max} (MPa)	204.00	241.17
[41]	G_{1c} (N/m)	43,600	43,600
	G_{2c} (N/m)	43,600	43,600
	G_{3c} (N/m)	43,600	43,600
[39]	c_1	0.001	0.001
	c_2	0	0
[42]	c_3	7.5×10^{-8}	30.0×10^{-8}
	c_4	1.75	1.25

3.4. *Fractography and fracture analysis*

The stress concentration caused by additive manufactured defects may cause the initiation and propagation of fatigue cracks under cyclic loading [47]. The surfaces of fatigue-fractured specimens were observed by SEM in order to further investigate the crack initiation. Fig. 13 shows the fracture surface of pure AlSi10Mg (Image a–a1) and 0.2AlSi10Mg/BNNS (Image b–b1) at low and high magnifications. It is evident that LMD-built pure AlSi10Mg specimen possesses multitude of interconnected pores and voids as shown in Fig. 13a. When a region is enlarged and shown at higher magnification in Fig. 13a1, the size of pores is in range 20–100 μm. Lack-of-fusion defect is also observed. The pores and lack-of-fusion defects are the dominant defects for crack initiation during the fatigue test of pure Al alloy. On the other hand, wrapping AlSi10Mg with BNNSs *via* wet-ball milling before LMD process promoted the compaction of microstructure. It is evident in Fig. 13b that adding BNNSs into LMD-built AlSi10Mg decreases the numbers of pores and voids on the fracture surface of 0.2AlSi10Mg/BNNS.

In fatigue loading, the crack is initiated and then propagated till fracture. Thus, it is highly dependent on internal

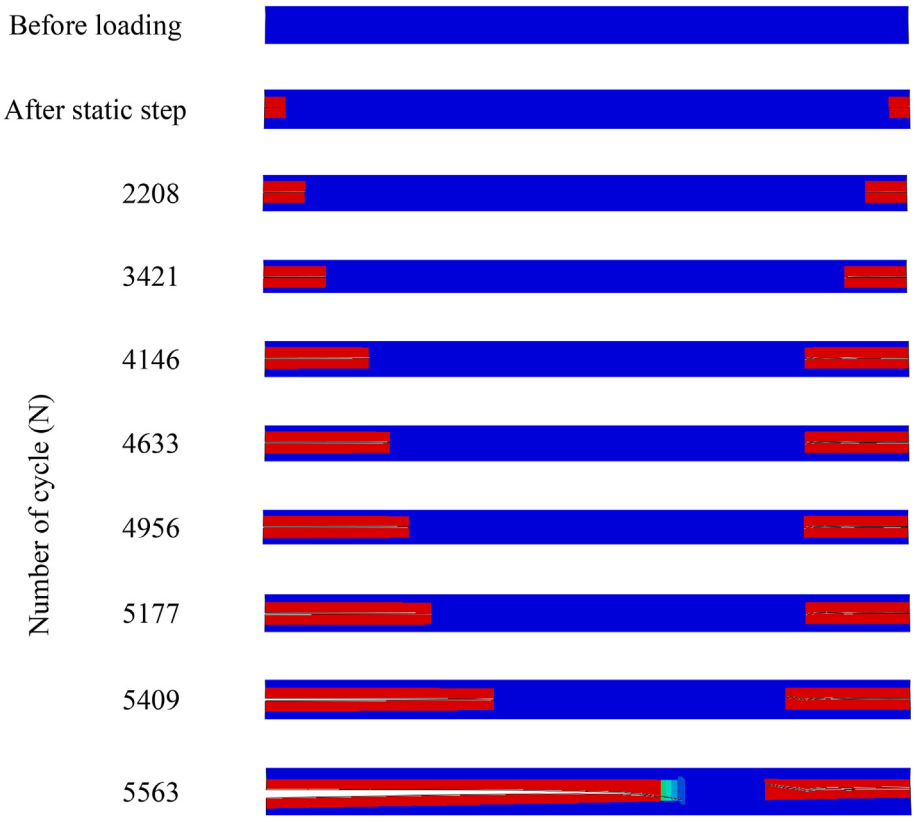

Fig. 11 – Crack propagation in pure AlSi10Mg subjected to cyclic loading *via* numerical model.

defects. Plate-like structure of BNNSs works as crack barrier to hinder the crack propagation provided that they are evenly distributed within the matrix. Therefore, 0.1 wt% was the optimum fraction. This fraction is very small so that it will not agglomerate and create stress concentration cites. However, 0.2 wt% does not have large increment relative to 0.1 wt%. This might be because BNNSs started to agglomerate at 0.2 wt% which was evident in SEM images in Fig. 5; BNNSs at 0.2 wt% did not firmly attach to the powder in comparison to those with 0.1 wt% BNNSs. Since all samples including pure Al alloy and its BNNS composites are fabricated by LMD, existence of BNNSs can be reason to reduce defects encountered during the LMD process. For example, the SEM micrographs in Fig. 13, the microstructure of pure Al alloy has high porosity in comparison with high dense and compact microstructure in Al alloy/BNNS composite. Therefore, the high increment of fatigue properties of LMD-built Al alloy/BNNS composite is because (i) the pure LMD-built Al alloy has low fatigue performance due to the porosity and lack-of-fusion defects; and (ii) the LMD-built Al alloy/BNNS composite has high fatigue properties due to better compact structure with less defects. According to the approximate relationship between micropore defects and fatigue limit deduced by Murakami and Endo [48], the size of micropore is inversely related to the ultimate strength of fatigue. This concludes that the addition of BNNSs into the AlSi10Mg matrix effectively reduced the size and number of micropores, strengthened the fatigue crack resistance promoting the number of cycles-to-failure.

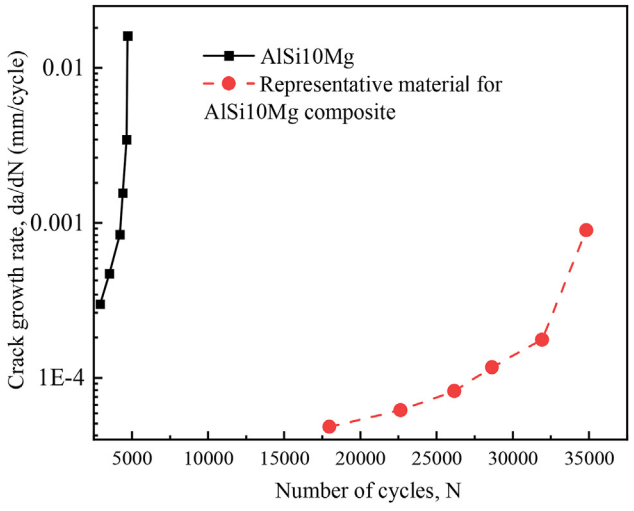

Fig. 12 – Crack growth rate (da/dN) *vs* number of cycles for AlSi10Mg and the material representing AlSi10Mg/BNNS composite.

When a selected region is enlarged to a high magnification as shown in Fig. 13b1, the typical fracture surface due to fatigue is observed. It is divided into three zones: (i) zone-I represents the area where the crack starts (blue dotted circle); (ii) zone-II shows crack propagation area (white dotted circle); and (iii) zone-III represents fracture region where failure or overload failure occurs. This observation is in accord with the work published in [49]. The white arrows indicate the direction of crack propagation. Zone-I was formed by an initial defect and the crack slowly propagated.

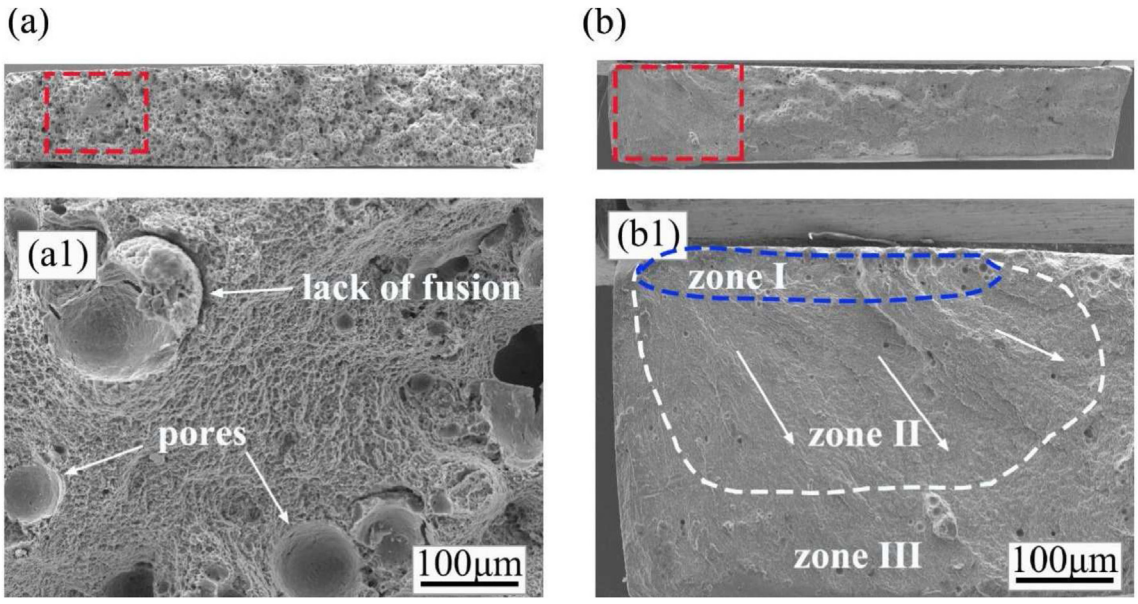

Fig. 13 – SEM images of fracture surface of fatigue-tested specimens: (a) AlSi10Mg alloy; (b) 0.2AlSi10Mg/BNNS, (a1) and (b1) are enlarged images of local red rectangles in (a) and (b), respectively. (For interpretation of the references to color in this figure legend, the reader is referred to the Web version of this article.)

Usually, various small cracks propagated on different planes and directions, then merged by ridges. Further investigation was performed by SEM at higher magnifications and different directions. Fig. 14 represents SEM micrographs from different regions of fracture surface of pure AlSi10Mg alloy and 0.2AlSi10Mg/BNNS. Several defects were detected where crack might have started. This includes internal pore in Fig. 14(a–b), melting pool in Fig. 14c, tearing (fatigue striation) in Fig. 14d and lack-of-fusion (inclusion) in Fig. 14(e–f).

According to literature, crack can be initiated from internal pores during the high cyclic fatigue regime [49]. Melting pool defect is usually found at the instantaneous fracture regions as shown in Fig. 14c. The molten pool is a fragile structure and its microstructure is discontinuous where the material was torn and cracks were initiated under cyclic stress [16]. With the crack propagation, the fatigue striation and ridges are developed due to the merging of fatigue cracks. Apparently, a layer of material was torn and the internal material

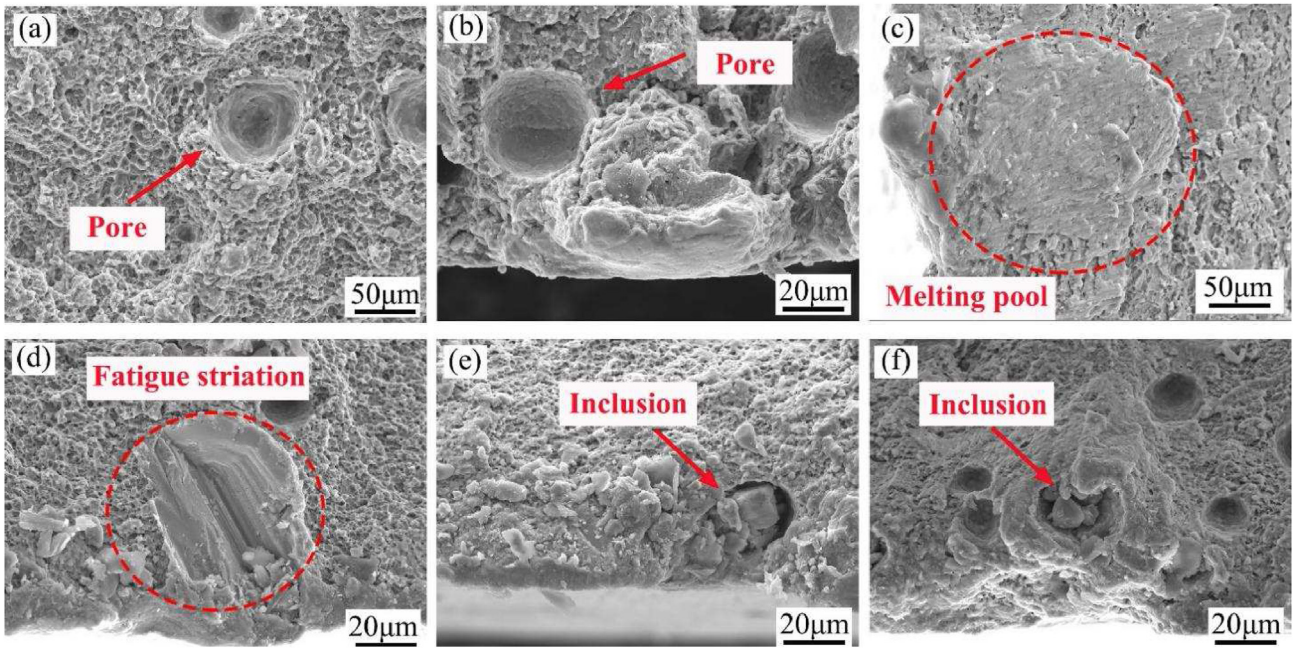

Fig. 14 – Defects of LMD-built Al alloy/BNNS composites: (a) and (b) internal pore of pure Al alloy, (c) and (d) tears of 0.2 wt% AiSi10Mg/BNNSs, (e) and (f) lack-of-fusion of 0.2 wt% AiSi10Mg/BNNSs.

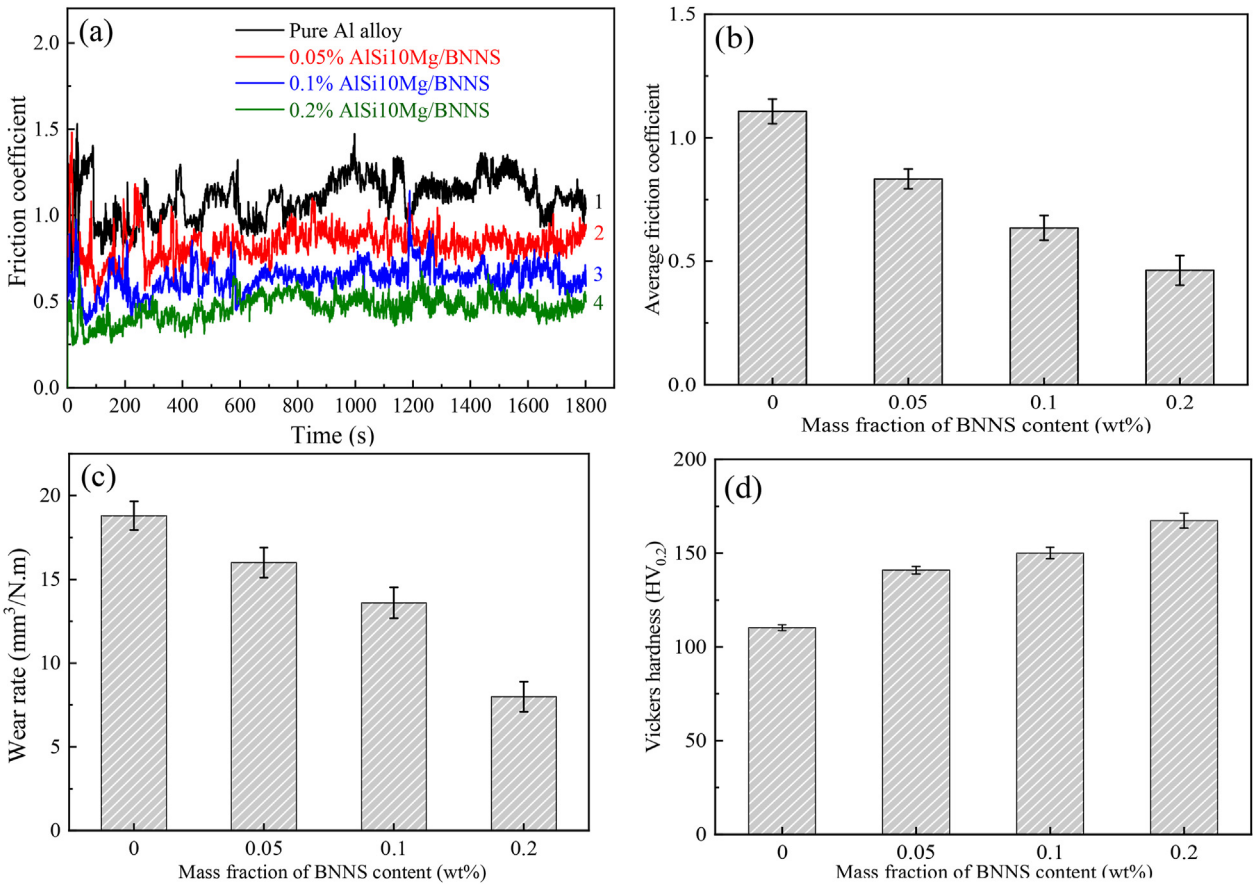

Fig. 15 – (a) Friction coefficient curves of AlSi10Mg/BNNS composites under bearing load of 5 N and 200 rpm for 1800 s; (b–c) average friction coefficient and wear rate of the composites *vs* BNNS content under bearing load of 5 N and 200 rpm; and (d) Vickers hardness of composites versus BNNS content.

was exposed. Lastly, the most frequent pattern of failure in the specimens was lack of fusion defect, as shown in Fig. 14(e–f) by red arrow. This failure started at all three locations, surface, subsurface and internal.

3.5. *Tribological properties of LMD-built AlSi10Mg/BNNS composite*

The evolution of friction coefficient, wear volume loss and wear rate of LMD-built samples from pure AlSi10Mg and AlSi10Mg/BNNS composites are presented in Fig. 15. In Fig. 15a, Curve 1 shows that pure AlSi10Mg alloy possesses high friction coefficient at a wide range of fluctuation. Curves (2–4) show lower values of friction coefficient within small range of variation upon adding BNNSs into the AlSi10Mg alloy. For example, in Table 7 the average friction coefficient of 0.2AlSi10Mg/BNNS composite is 0.46 in comparison with 1.11 for pure Al alloy recording 2.4-fold reduction. Wear volume loss and wear rate of the composite decreased significantly with the addition of BNNSs as presented in Table 7 and Fig. 15c. For example, wear volume loss decreased by 57% when 0.2 wt% BNNSs was added into Al alloy. The wear rate was reduced from 18.8 mm^3/Nm for pure Al alloy to 8 mm^3/Nm in case of 0.2AlSi10Mg/BNNS composite.

It is known that hexagonal boron nitride has a lubricant characteristic with high thermal stability due to its layer structure. Therefore, it is often used as a high temperature lubricant additive [50,51]. In the course of wear test, when pure Al alloy was tested, metal-to-metal friction is occurred showing high friction coefficient, wear loss and wear rate. After 800 s, the friction coefficient largely fluctuates between 1.2 and 1.5 as presented in Fig. 15, Curve 1. This is due to the increase in the generated heat during the test between Al–alloy and the substrate. This would melt a thin layer at the contact surface of Al alloy and hence it experiences a stick-and-slip phenomena between the contact surfaces leading to high friction coefficient with large fluctuation.

Table 7 – Effect of BNNSs on friction coefficient and wear volume of AlSi10Mg composites under test of 5 N with 200 rpm.

BNNS content (wt %)	Average friction coefficient	Wear volume loss (mm^3)	Wear rate (mm^3/Nm)
0	1.11	0.47	18.8
0.05	0.83	0.40	16
0.1	0.64	0.34	13.6
0.2	0.46	0.20	8

Table 8 – Tribological properties of AMCs prepared by conventional methods.

Preparation method	Matrix material	Filler type	Friction coefficient (reduction %)	Wear rate (reduction %)	Wear loss (reduction %)	Ref.
Vortex method	2024 Al alloy	Al_2O_3 microparticle	/	/	99	[54]
Stir casting	7079 Al alloy	TiC particulate	18	/	40	[7]
Friction-stir processing	AA7075 Al alloy	BN; SiC nanoparticles	/	22	/	[55]
Stir and squeeze casting	AA7050 Al alloy	graphene	23	7.3	/	[53]
Vacuum pressure infiltration	6061Al alloy	short carbon fibers	55	/	99	[56]
Spray forming technique	Al–6Si alloy	Graphite particulates	33	93	80	[57]
Stir casting	AA1100 Al alloy	TiB_2 microparticle	/	52	83	[52]
Stir casting	LM4 Al alloy	WC particles	47.3	66	/	[58]
Spark plasma sintering	Al	Ni-CNTs	18.4	/	74.2	[59]
Laser metal deposition	AlSi10Mg alloy	Boron nitride nanosheets	58	57.44	57	This work

On the other hand, when BNNSs is added, the AlSi10Mg/BNNS composites starts with high friction coefficient (still lower than pure Al alloy). After short time, under the action of reciprocating load, the surface of composites exhibited plastic deformation. BNNSs were extruded from the sliding surface and ground into fine fragments. These fragments diffused between the composite and substrate forming a lubricant-thin film which facilitated the Al–alloy composite to slide over the substrate with low coefficient of friction. The more BNNSs in the composite, the better lubricant layer is formed leading to constant and low friction coefficient, low wear loss and low wear rate. Therefore, BNNSs can offset the onset of plastic deformation of the Al alloy with high capacity for bearing loads. Moreover, adding stiff material like BNNSs to Al–alloy improves the hardness of the matrix. The Vickers hardness of AlSi10Mg increases from 110 to 167 HV when 0.2 wt% BNNSs is added. This consequently promotes the wear resistance of AlSi10Mg alloy.

Table 8 shows a comparison between the LMD-fabricated AlSi10Mg alloy and other Al alloys fabricated by vortex method, casting, friction-stir processing. Although ceramic particles endow AMCs better wear properties in comparison with pure Al alloy, they are added at high filler content. For example, 30 wt% TiB_2 microparticle can reduce wear rate and wear loss of Al alloy by 52% and 83%, respectively [52]. Adding 9 wt% TiC into Al alloy drops friction coefficient by 18% and reduces wear volume loss by 40% [7]. When graphene was used as a reinforcing phase to strengthen AMCs *via* stir and squeeze casting, the friction coefficient and wear rate decreased by 23% and 7.3%, respectively [53]. In the present work, when only 0.2 wt% BNNS was added into Al alloy *via* LMD process, the friction coefficient, wear rate and wear loss of composites respectively decreased by 58%, 57.44% and 57%.

3.6. *Wear mechanism*

Further investigation was conducted using SEM imaging on the wear surface of LMD-built Al ally/BNNS composites. Fig. 16 shows the SEM micrographs of the wear surfaces of pure AlSi10Mg and AlSi10Mg/BNNS composites under wear conditions of 5 N and 200 rpm. The wear surface of pure Al alloy composed of grooves, wide ridges and debris inside the grooves with large protrusions of worn material along the groove edges as in Fig. 16(a–a1). The wear surface is highly rough with features of plastic deformation and delamination on the wear trails. The protrusions and debris are mainly due to the extrusion and shear effects of the friction pair on the cladding surface. This results in an outward accumulation of worn material at the wear-track edges. As mentioned before, the microstructure of the sample prepared by LMD is composed of coarse α-Al dendrite and Al–Si eutectic distributed along the grain boundary. In the process of wear, low hardness α-Al dendrite was plastically deformed while the coarse Al–Si eutectic particles had a serious cutting effect on the surface forming layered steps surface. In pure Al alloy, there are two factors are activated: (i) hardening and partial oxidation occurred under repeated deformation, and (ii) some material was peeled off due to shear stress.

On the other hand, 0.05AlSi10Mg/BNNS sample shows relatively wider and shallower grooves on the wear surface in comparison with pure AlSi10Mg which is a sign of low wear rate, as shown in Fig. 16(b–b1). With the increase of BNNS content, the wear surface becomes less rough with clearer sliding paths as shown in Fig. 16(c–c1) and (d–d1). Small number of pressure pits and shallow grooves are observed in those figures. It is evident that adding relatively large content of BNNSs such as 0.2 wt% into Al alloy suppresses stick-and-slip phenomena or adhesion during the wear test. This is evident in Fig. 16d1 which shows stable and clear sliding paths in Al–alloy/BNNS composite. Moreover, debris or protrusions are not observed. Fig. 17 shows quantitively wear depth and width of the prepared composites after the wear test. Pure AlSi10Mg has deep and sharp groove with ~120 μm depth as presented in Fig. 17a. In Fig. 17(b–d), the wear depth of 0.05AlSi10Mg/BNNS, 0.1AlSi10Mg/BNNS and 0.2AlSi10Mg/BNNS are much less than of pure AlSi10Mg. The 0.2AlSi10Mg/BNNS sample recorded ~55 μm as in Fig. 17d. These measurements are consistent with the values of wear loss and wear rate provided in Table 7.

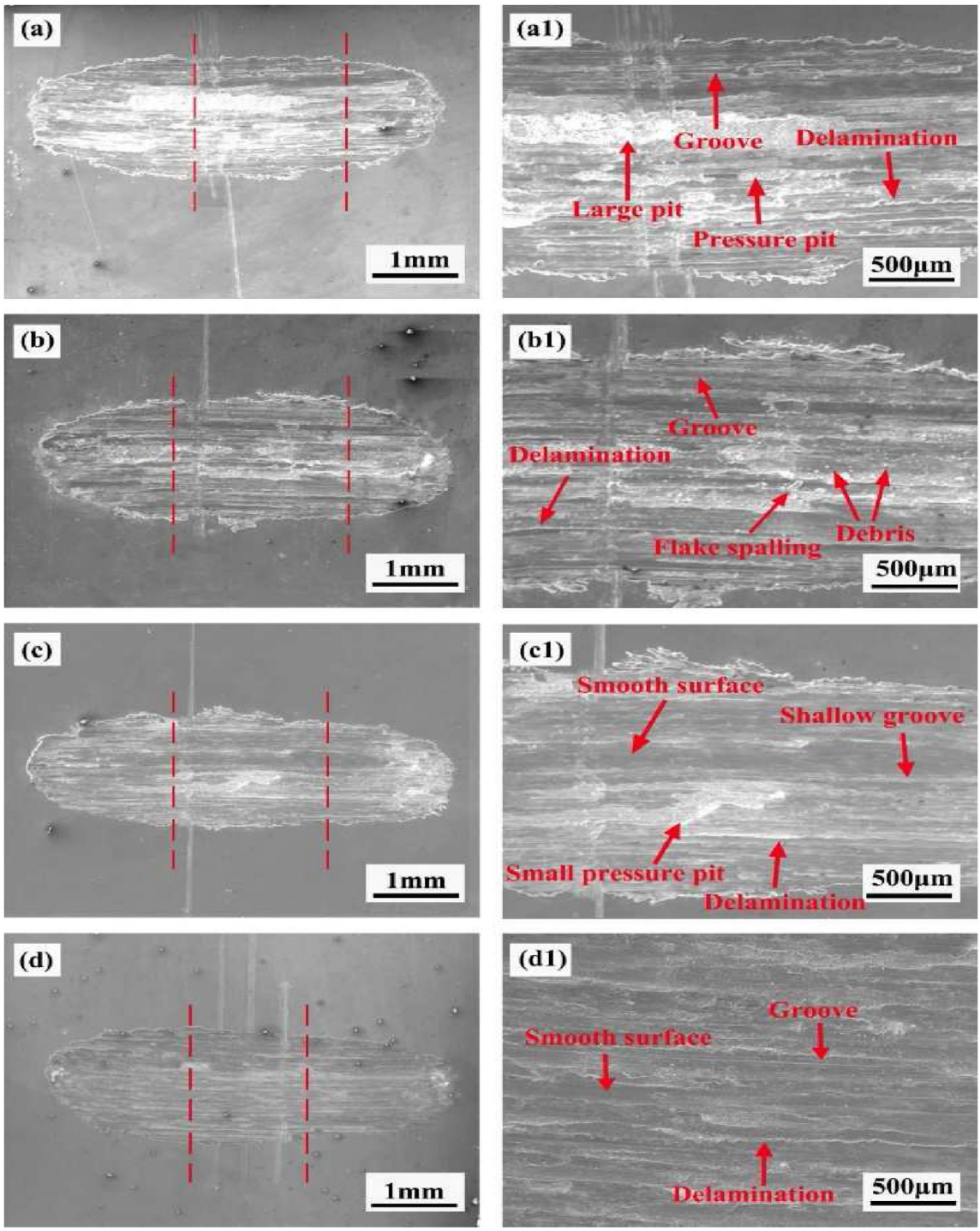

Fig. 16 – Wear surfaces of the composites tested under 5 N with 200 rpm: (a) pure AlSi10Mg alloy, (b) 0.05AlSi10Mg/BNNS, (c) 0.1AlSi10Mg/BNNS and (d) 0.2AlSi10Mg/BNNS; and (a1–d1) are enlarged images of the area between the red lines in their corresponding micrographs, respectively. (For interpretation of the references to color in this figure legend, the reader is referred to the Web version of this article.)

3.7. *The effect of wear load and sliding speed*

Table 9 presents the measurements of friction coefficient and wear loss of 0.2AlSi10Mg/BNNS composite at different bearing load and sliding speed. The Al alloy/BNNS composite experienced large amount of wear loss with the increase of bearing load or sliding speed. At sliding speed of 200 rpm, the wear loss significantly increased by 6.2 folds when the bearing load increased from 5 to 20 N. This increment was marginally the same when the sliding speed was 500 rpm. At 5 N bearing load, the wear loss increased from 0.2 mm^3 at 200 rpm to 0.53 mm^3 at 20 N. The friction coefficient increased in similar

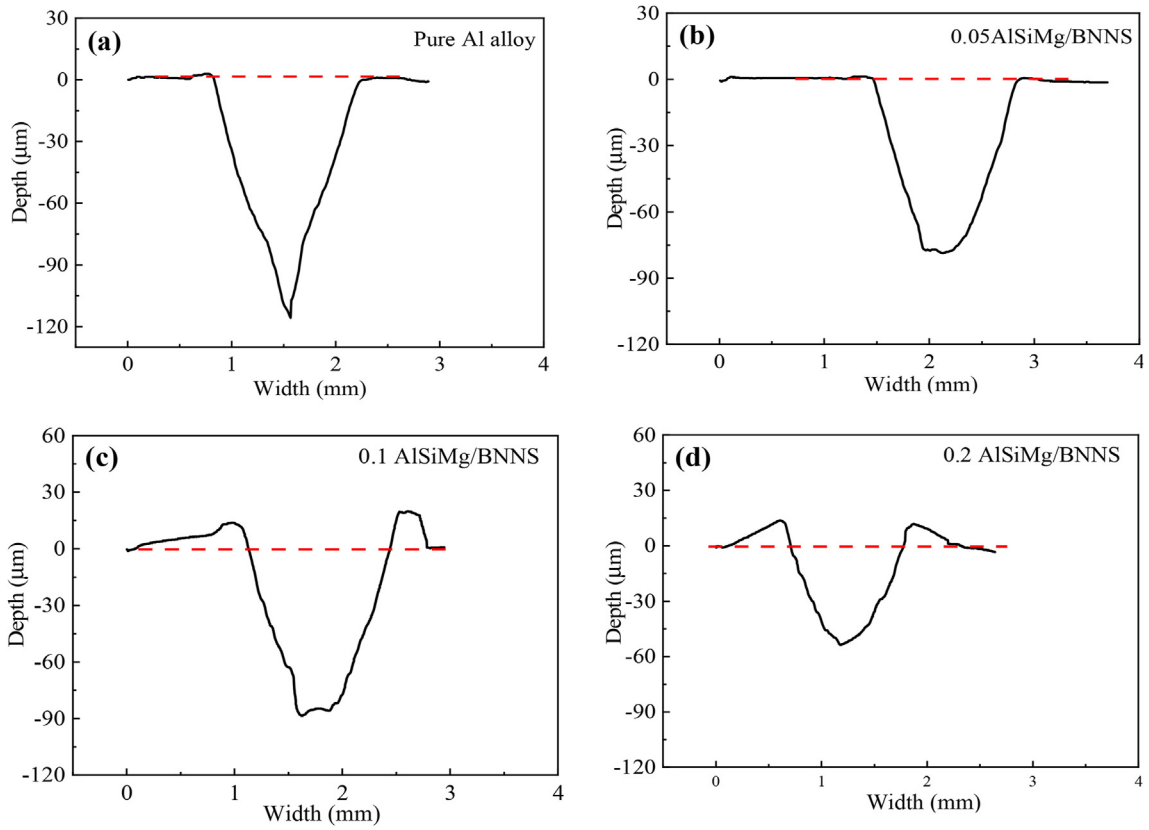

Fig. 17 – Wear depth curve of composites at various BNNS contents under 5 N and 200 rpm.

manner with the increase of bearing load or sliding speed. This is because the high load and sliding speed impose severe plastic deformation on 0.2AlSi10Mg/BNNS composite. With the increase of bearing load and sliding speed, the plastic deformation on the worn surface was aggravated. When the external force is at certain level, the plastic deformation layer broke down transferring fragments into debris which can work as micro cutting tools and thus scratch the surface.

SEM micrographs of the wear surfaces of 0.2AlSi10Mg/BNNS are shown in Fig. 18 at various sliding speed and bearing load. At 500 rpm and load of 5 N, the slideways are clear with shallow grooves and ridges as presented in Fig. 18a. Plastic deformation is high in the middle of the wear surface where the bearing force tip is concentrated. Also, delamination is observed. When the bearing load is increased to 20 N, large spalling crater is observed on the wear surface as shown in Fig. 18b. Plastic deformation and debris are obvious throughout the entire surface due to severe extrusion and tearing. A typical adhesion wear is also presented on the surface. When the load remained at 20 N while the sliding speed increased from 200 to 500 rpm, the wear surface is wider and deeper spalling craters as displayed in Fig. 18(c–d). It also shows multitude of wear debris at high speed in comparison with slight pressure pits and few patches at low speed. Although the BNNS content is at the highest value (0.2 wt%), it is not enough to create a complete lubricant layer to protect the composite from wear due to friction at this relatively high load.

Table 9 – Tribological properties of 0.2AlSi10Mg/BNNS composites at different loads and sliding velocities.

Sliding velocity (rpm)	Load (N)	Friction coefficient	Wear volume loss (mm^3)
200 rpm	5	0.42	0.20
	20	0.82	1.238
500 rpm	5	0.7735	0.5345
	20	0.9865	2.7865

4. Conclusion

In this study, we explored the application of additive manufacturing in synthesis Al nanocomposites with high fatigue performance and wear resistance using boron nitride nanosheets (BNNSs). The Al alloy/BNNS nanocomposites were prepared by laser metal deposition (LMD). The fatigue performance and tribological properties of Al alloy (AlSi10Mg) reinforced with BNNSs at low mass fractions (0–0.2 wt%) were measured and investigated. The following conclusions can be drawn:

1. Al alloy powder was wrapped and coated with BNNSs *via* high-energy wet ball-milling. Good dispersion and adhesion of BNNSs onto AlSi10Mg powder were evident by SEM and EDS analysis.
2. The addition of BNNSs improves the microstructure of the Al alloy composites. Compared to pure AlSi10Mg, the microstructure of Al–Si eutectic and α-Al becomes finer

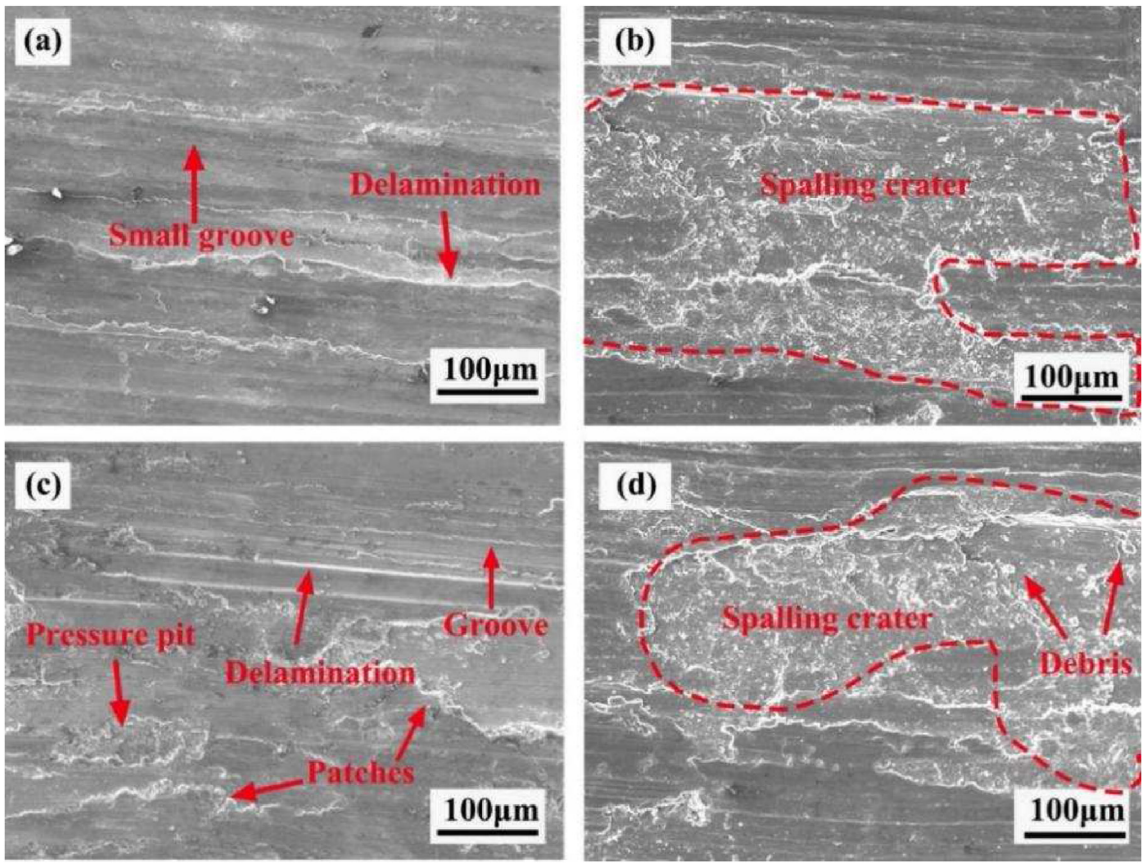

Fig. 18 – Wear surface of the 0.2 AlSi10Mg/BNNS composites tested at (a) 500 rpm and 5 N, (b) 500 rpm and 20 N, (c) 200 rpm and 20 N and (d) 500 rpm and 20 N.

and denser, which is conducive to the enhancement of Al matrix by grain refinement.

3. The addition of BNNSs improved the fatigue performance of the Al alloy. The number of cycles-to-failure increased from 5×10^4 for pure AlSi10Mg to 1×10^6 upon adding only 0.1 wt% BNNSs.
4. The fracture morphology after fatigue testing revealed typical fatigue failure progression: crack initiation, crack propagation and final fracture. Large number and size of pores appeared at the fracture surface of pure Al alloy while Al alloy/BNNS composite showed compact and dense fracture surface after fatigue failure. The improvement of fatigue life with the addition of BNNSs was also presented using extended finite element model and qualitatively showed a similar trend to the fatigue measurements.
5. AlSi10Mg/BNNS composites with excellent tribological properties was successfully prepared by LMD technology. With the addition of BNNSs, the average friction coefficient and wear rate of the composite decrease significantly. The composite has a smoother surface and smaller wear marks than the pure Al surface.
6. The friction coefficient and wear-out volume of AlSi10Mg alloy reduced by 58% and 57%, respectively when 0.2 wt% BNNSs is added. The wear mechanism in pure AlSi10Mg is mainly plastic deformation, delamination and adhesion. The LMD-built AlSi10Mg/BNNS composites exhibited clear wear trails due to the thin lubricant layer formed from the extruded BNNSs during the wear test.

Funding

This work was financially supported by the Open Fund of Key Laboratory of Fundamental Science for Aeronautical Digital Manufacturing Process of Shenyang Aerospace University (SHSYS201905) and the plan of rejuvenating the Talents of Liaoning Province (XLYC1907135). Social Policy Grant, Nazarbayev University.

Data availability

The raw/processed data required to produce these finding is part of and available within the manuscript.

Declaration of competing interest

The authors declare that they have no known competing financial interests or personal relationships that could have appeared to influence the work reported in this paper.

REFERENCES

[1] Kaczmar JW, Pietrzak K, WłOsiński W. The production and application of metal matrix composite materials. J Mater Process Technol 2000;106(1–3):58–67. https://doi.org/10.1016/S0924-0136(00)00639-7.

[2] Rawal SP. Metal-matrix composites for space applications. J Miner Metal Mater Soc 2001;53(4):14–7. https://doi.org/10.1007/s11837-001-0139-z.

[3] Koli DK, Agnihotri G, Purohit R. Advanced aluminium matrix composites: the critical need of automotive and aerospace engineering fields. Mater Today Proc 2015;2(4–5):3032–41. https://doi.org/10.1016/j.matpr.2015.07.290.

[4] Cheng W, Liu Y, Xiao X, Huang B, Zhou Z, Liu X. Microstructure and mechanical properties of a novel (TiB_2+TiC)/AlSi10Mg composite prepared by selective laser melting. Mater Sci Eng 2022:834. https://doi.org/10.1016/j.msea.2021.142435.

[5] Li XP, Ji G, Chen Z, Adda DA, Wu Y, Wang HW, et al. Selective laser melting of nano-TiB2 decorated AlSi10Mg alloy with high fracture strength and ductility. Acta Mater 2017;129(Complete):183–93. https://doi.org/10.1016/j.actamat.2017.02.062.

[6] Gao C, Wu W, Shi J, Xiao Z, Akbarzadeh AH. Simultaneous enhancement of strength, ductility, and hardness of TiN/AlSi10Mg nanocomposites via selective laser melting. Addit Manuf 2020;34. https://doi.org/10.1016/j.addma.2020.101378.

[7] Sujith SV, Mahapatra MM, Mulik RS. Microstructural characterization and experimental investigations into two body abrasive wear behavior of Al-7079/TiC in-situ metal matrix composites. Proc IME J J Eng Tribol 2019;234(4):588–607. https://doi.org/10.1177/1350650119883559.

[8] Liu K, Li Y, Duan M-g, Zhang T, Li C, Li B. Fatigue life prediction of in-situ TiB2/2024 aluminum matrix composite. Int J Fatig 2021:145. https://doi.org/10.1016/j.ijfatigue.2020.106128.

[9] Karthik GM, Panikar S, Ram GDJ, Kottada RS. Additive manufacturing of an aluminum matrix composite reinforced with nanocrystalline high-entropy alloy particles. Mater Sci Eng, A 2017;679:193–203. https://doi.org/10.1016/j.msea.2016.10.038.

[10] Xi X, Chen B, Tan C, Song X, Feng J. Microstructure and mechanical properties of SiC reinforced AlSi10Mg composites fabricated by laser metal deposition. J Manuf Process 2020;58:763–74. https://doi.org/10.1016/j.jmapro.2020.08.073.

[11] Wang T, Meng Q, Araby S, Yang G, Li P, Cai R, et al. Non-oxidized graphene/metal composites by laser deposition additive manufacturing. J Alloys Compd 2021;882:160724. https://doi.org/10.1016/j.jallcom.2021.160724.

[12] Ngo TD, Kashani A, Imbalzano G, Nguyen KTQ, Hui D. Additive manufacturing (3D printing): a review of materials, methods, applications and challenges. Compos B Eng 2018;143:172–96. https://doi.org/10.1016/j.compositesb.2018.02.012.

[13] Li P, Cai R, Yang G, Wang T, Han S, Zhang S, et al. Mechanically strong, stiff, and yet ductile AlSi7Mg/graphene composites by laser metal deposition additive manufacturing. Mater Sci Eng 2021;823:141749. https://doi.org/10.1016/j.msea.2021.141749.

[14] Tiwari JK, Mandal A, Sathish N, Kumar S, Ashiq M, Nagini M, et al. Effect of graphene addition on thermal behavior of 3D printed graphene/AlSi10Mg composite. J Alloys Compd 2022;890:161725. https://doi.org/10.1016/j.jallcom.2021.161725.

[15] Ferro P, Fabrizi A, Berto F, Savio G, Meneghello R, Rosso S. Defects as a root cause of fatigue weakening of additively manufactured AlSi10Mg components. Theor Appl Fract Mech 2020;108. https://doi.org/10.1016/j.tafmec.2020.102611.

[16] Xu ZW, Wang Q, Wang XS, Tan CH, Guo MH, Gao PB. High cycle fatigue performance of AlSi10mg alloy produced by selective laser melting. Mech Mater 2020:148. https://doi.org/10.1016/j.mechmat.2020.103499.

[17] Cazorla C, Gould T. Polymorphism of bulk boron nitride. Sci Adv 2019;5(1). https://doi.org/10.1126/sciadv.aau5832.

[18] Chen X, Dmuchowski CM, Park C, Fay CC, Ke C. Quantitative characterization of structural and mechanical properties of boron nitride nanotubes in high temperature environments. Sci Rep 2017;7(1):11388. https://doi.org/10.1038/s41598-017-11795-9.

[19] Kumar S. Selective laser sintering/melting. Compr Mater Process 2014:93–134. https://doi.org/10.1016/B978-0-08-096532-1.01003-7.

[20] Yasin MS, Soltani-Tehrani A, Shao S, Haghshenas M, Shamsaei N. A comparative study on fatigue performance of various additively manufactured titanium alloys. Procedia Struct Integr 2022;38:519–25. https://doi.org/10.1016/j.prostr.2022.03.052.

[21] Tridello A, Fiocchi J, Biffi CA, Chiandussi G, Rossetto M, Tuissi A, et al. Influence of the annealing and defects on the VHCF behavior of an SLM AlSi10Mg alloy. Fatig Fract Eng Mater Struct 2019;42(12). https://doi.org/10.1111/ffe.13123.

[22] Du Y, Wang X, Zhang D, Wang X, Ju C, Jiang B. A superior strength and sliding-wear resistance combination of ductile iron with nanobainitic matrix. J Mater Res Technol 2021;11:1175–83. https://doi.org/10.1016/j.jmrt.2021.01.104.

[23] Kim SM, Hsu A, Park MH, Chae SH, Yun SJ, Lee JS, et al. Synthesis of large-area multilayer hexagonal boron nitride for high material performance. Nat Commun 2015;6:8662. https://doi.org/10.1038/ncomms9662.

[24] Park JH, Park JC, Yun SJ, Kim H, Luong DH, Kim SM, et al. Large-area monolayer hexagonal boron nitride on Pt foil. ACS Nano 2014;8(8):8520–8. https://doi.org/10.1021/nn503140y.

[25] Song L, Ci L, Lu H, Sorokin PB, Jin C, Ni J, et al. Large scale growth and characterization of atomic hexagonal boron nitride layers. Nano Lett 2010;10(8):3209–15. https://doi.org/10.1021/nl1022139.

[26] Wang S, Xue H, Araby S, Demiral M, Han S, Cui C, et al. Thermal conductivity and mechanical performance of hexagonal boron nitride nanosheets-based epoxy adhesives. Nanotechnology 2021;32(35):355707. https://doi.org/10.1088/1361-6528/ac0470.

[27] Zhao Z, Bai P, Misra RDK, Dong M, Guan R, Li Y, et al. AlSi10Mg alloy nanocomposites reinforced with aluminum-coated graphene: selective laser melting, interfacial microstructure and property analysis. J Alloys Compd 2019;792:203–14. https://doi.org/10.1016/j.jallcom.2019.04.007.

[28] Lv F, Shen L, Liang H, Xie D, Wang C, Tian Z. Mechanical properties of AlSi10Mg alloy fabricated by laser melting deposition and improvements via heat treatment. Optik 2019;179:8–18. https://doi.org/10.1016/j.ijleo.2018.10.112.

[29] Demir AG, Biffi CA. Micro laser metal wire deposition of thin-walled Al alloy components: process and material characterization. J Manuf Process 2019;37:362–9. https://doi.org/10.1016/j.jmapro.2018.11.017.

[30] Yu H, Dong Q, Yang C, Chen C. Influence of silicon on growth mechanism of micro-arc oxidation coating on cast Al–Si alloy. R Soc Open Sci 2018;5(7):172428. https://doi.org/10.1098/rsos.172428.

[31] Cauwenbergh PV, Samaee V, Thijs L, Nejezchlebová J, Vanmeensel. Unravelling the multi-scale structure–property relationship of laser powder bed fusion processed and heat-

treated AlSi10Mg. Sci Rep 2021;11(1). https://doi.org/10.1038/s41598-021-85047-2.
[32] Hochreiter E, Panzenböck M, Jeglitsch F. Fatigue properties of particle-reinforced metal-matrix composites. Int J Fatig 1993;15(6):493–9. https://doi.org/10.1016/0142-1123(93)90262-O.
[33] Divagar S, Vigneshwar M, Selvamani ST. Impacts of nano particles on fatigue strength of aluminum based metal matrix composites for aerospace. Mater Today Proc 2016;3(10):3734–9. https://doi.org/10.1016/j.matpr.2016.11.021.
[34] Koh SK, Oh SJ, Li C. Low-cycle fatigue life of SiC-particulate-reinforced Al-Si cast alloy composites with tensile mean strain effects. Int J Fatig 1999;21(10):1019–32. https://doi.org/10.1016/S0142-1123(99)00099-7.
[35] Zhang Z, Zhao Y, Wang C, Tao R, Fang Z, Sun Y, et al. High cycle fatigue behavior of in-situ ZrB_2/AA6111 composites. Mater Sci Eng 2020:788. https://doi.org/10.1016/j.msea.2020.139590.
[36] Zolfaghari M, Azadi M, Azadi M. Characterization of high-cycle bending fatigue behaviors for piston aluminum matrix SiO_2 nano-composites in comparison with aluminum–silicon alloys. Int J Metalcast 2020;15(3):1–17. https://doi.org/10.1007/s40962-020-00437-y.
[37] Kouka MA, Abbassi F, Demiral M, Ahmad F, Soula M, Housni FA. Behaviour of woven-ply PPS thermoplastic laminates with interacting circular holes under tensile loading: an experimental and numerical study. Eng Fract Mech 2021;251:107802. https://doi.org/10.1016/j.engfracmech.2021.107802.
[38] Systèmes D. Abaqus 6.12 Online documentation. 2012.
[39] Gupta RS, Xin H, Veljkovic M. Fatigue crack propagation simulation of orthotropic bridge deck based on extended finite element method. Procedia Struct Integr 2019;22:283–90. https://doi.org/10.1016/j.prostr.2020.01.036.
[40] Ali Kouka M, Abbassi F, Demiral M, Ahmad F, Soula M, Al Housni F. Behaviour of woven-ply PPS thermoplastic laminates with interacting circular holes under tensile loading: an experimental and numerical study. Eng Fract Mech 2021;251:107802. https://doi.org/10.1016/j.engfracmech.2021.107802.
[41] Nirmal RR, Patnaik B, Jayaganthan R. FEM simulation of high speed impact behaviour of additively manufactured AlSi10Mg alloy. J Dyn Behav Mater 2021;7(3):469–84. https://doi.org/10.1007/s40870-020-00285-1.
[42] Giovanni M, Menezes J, Bolelli G, Cerri E, Castrodeza EM. Fatigue crack growth behavior of a selective laser melted AlSi10Mg. Eng Fract Mech 2019;217:106564. https://doi.org/10.1016/j.engfracmech.2019.106564.
[43] Bomidi J, Weinzapfel N, Wang CP, Sadeghi F. Experimental and numerical investigation of fatigue of thin tensile specimen. Int J Fatig 2012;44:116–30. https://doi.org/10.1016/j.ijfatigue.2012.05.013.
[44] Liu HY, Wang G, Mai YW. Cyclic fatigue crack propagation of nanoparticle modified epoxy. Compos Sci Technol 2012;72(13):1530–8. https://doi.org/10.1016/j.compscitech.2012.05.025.
[45] Gairola S, Jayaganthan R. XFEM simulation of tensile and fracture behavior of ultrafine-grained Al 6061 alloy. Metals 2021;11(11):1761. https://doi.org/10.3390/met11111761.
[46] Teimouri F, Heidari-Rarani M, Aboutalebi FH. An XFEM-VCCT coupled approach for modeling mode I fatigue delamination in composite laminates under high cycle loading. Eng Fract Mech 2021;249:107760. https://doi.org/10.1016/j.engfracmech.2021.107760.
[47] Kim Dong-Kyu, Hwang Ji-Hyun, Kim Eun-Young, Heo Yoon-Uk, Wanchuck Woo, Choi Shi-Hoon, et al. Evaluation of the stress-strain relationship of constituent phases in AlSi10Mg alloy produced by selective laser melting using crystal plasticity FEM. J Alloys Compd 2017;714(15):687–97. https://doi.org/10.1016/j.jallcom.2017.04.264.
[48] Murakami Y, Endo M. Effects of defects, inclusions and inhomogeneities on fatigue strength. Int J Fatig 1994;16(3):163–82. https://doi.org/10.1016/0142-1123(94)90001-9.
[49] Qian G, Jian Z, Qian Y, Pan X, Ma X, Hong Y. Very-high-cycle fatigue behavior of AlSi10Mg manufactured by selective laser melting: effect of build orientation and mean stress. Int J Fatig 2020:138. https://doi.org/10.1016/j.ijfatigue.2020.105696.
[50] Charoo MS, Wani MF. Tribological properties of h-BN nanoparticles as lubricant additive on cylinder liner and piston ring. Lubric Sci 2016;29(4):241–54. https://doi.org/10.1002/ls.1366.
[51] Zhao J, Chen G, He Y, Li S, Duan Z, Li Y, et al. A novel route to the synthesis of an Fe_3O_4/h-BN 2D nanocomposite as a lubricant additive. RSC Adv 2019;9. https://doi.org/10.1039/C8RA10312G.
[52] Tee KL, Lu L, Lai MO. Wear performance of in-situ Al–TiB_2 composite. Wear 2000;240(1–2):59–64. https://doi.org/10.1016/S0043-1648(00)00337-9.
[53] Venkatesan S, Anthony Xavior M. Wear property evaluation of aluminum alloy (AA7050) metal matrix composite reinforced with graphene fabricated by stir and squeeze cast processes. Mater Today Proc 2020;22:3330–9. https://doi.org/10.1016/j.matpr.2020.03.296.
[54] Kok M, Ozdin K. Wear resistance of aluminium alloy and its composites reinforced by Al_2O_3 particles. J Mater Process Technol 2007;183(2–3):301–9. https://doi.org/10.1016/j.jmatprotec.2006.10.021.
[55] Moustafa EB, Melaibari A, Basha M. Wear and microhardness behaviors of AA7075/SiC-BN hybrid nanocomposite surfaces fabricated by friction stir processing. Ceram Int 2020;46(10):16938–43. https://doi.org/10.1016/j.ceramint.2020.03.274.
[56] Liu L, Li W, Tang Y, Shen B, Hu W. Friction and wear properties of short carbon fiber reinforced aluminum matrix composites. Wear 2009;266(7–8):733–8. https://doi.org/10.1016/j.wear.2008.08.009.
[57] Chourasiya SK, Gautam G, Singh D. Influence of rolling on wear and friction behaviour of spray formed Al alloy composites. Mater Today Proc 2020;28:813–8. https://doi.org/10.1016/j.matpr.2019.12.304.
[58] Sharath Kumar PN, Sachit TS, Mohan N, AkshayPrasad M. Dry sliding wear behaviour of Al –5Si-3Cu-0.5Mn alloy and its WC reinforced composites at elevated temperatures. Mater Today Proc 2021;44:566–72. https://doi.org/10.1016/j.matpr.2020.10.351.
[59] Murugesan R, Gopal M, Murali G. Effect of Cu, Ni addition on the CNTs dispersion, wear and thermal expansion behavior of Al-CNT composites by molecular mixing and mechanical alloying. Appl Surf Sci 2019;495. https://doi.org/10.1016/j.apsusc.2019.143542.